J. Fluid Mech. (1998), *vol.* 358, *pp.* 29–60 Printed in the United Kingdom

Experiments on collapsing turbulent regions in stratified fluids

By I. P. D. DE SILVA† AND H. J. S. FERNANDO

Environmental Fluid Dynamics Program, Department of Mechanical and Aerospace Engineering, Arizona State University, Tempe, AZ 85287-9809, USA

(Received 1 February 1996 and in revised form 12 October 1997)

Laboratory experiments were carried out to investigate the properties of a collapsing turbulent patch generated within a linearly stratified fluid by a sustained energy source and its long-time evolution in the presence of lateral boundaries. An oscillating grid spanning the width of the experimental tank was used as the turbulence source. Initially, the patch grows rapidly, as in an unstratified fluid, until the buoyancy forces arrest its vertical growth. Thereafter, the patch collapses to form horizontally propagating intrusions at its equilibrium density level. The fluid lost from the patch into the intrusion is replenished by return currents generated at the top and bottom edges of the patch. The nose of the intrusion propagates with a constant average speed ('initial spreading regime') determined mainly by the horizontal pressure gradient forces and the resistance induced by upstream propagating, low-frequency, columnar internal waves. Although the intrusion propagation speed is independent of viscous effects, they cause the development of a slug of fluid pushed ahead of the intrusion. When this slug reaches the endwall, strong upstream blocking occurs, causing the intrusion to decelerate ('blocked regime'); the intrusion nose, however, eventually reaches the endwall. The thickness of the patch is found to be approximately constant during the initial spreading regime and slowly growing in the blocked regime. At large times (t) both the patch and the 'fully blocked' intrusion begin to grow vertically with a power law of the form $t^{1/5}$. A simple mixing model is advanced to explain this observation. Various turbulent and internal-wave parameters pertinent to collapsing patches were also measured, and their properties were compared with those of non-collapsing patches.

1. Introduction

Studies on turbulent patches are of importance because of growing laboratory, oceanic and atmospheric evidence that turbulence in stratified media is confined to isolated patches. Illustrative laboratory experiments by McEwan (1983) show that these patches take the form of thin, horizontally elongated, mixed regions. Patches observed in geophysical situations also have a similar appearance. The origin of oceanic patches may be due to mechanisms such as internal-wave breakdown due to local shear (Marmorino 1987*a*), critical-layer absorption (Broutman 1986), near-inertial wave shear (Gregg 1984), Kelvin–Helmholtz instabilities (Woods 1968), boundary mixing (Armi 1978) or double-diffusive instabilities (Marmorino 1987*b*), while patchy turbulence in the atmosphere is usually attributed to internal-wave breaking or Kelvin–Helmholtz billows (Caughey 1982). Although it is generally agreed

† Present address: Department of Mechanical Engineering, Sirindhorn International Institute of Technology, Thammasat University, PO Box 22, Pathumthani 12121, Bangkok.

that atmospheric patches are sporadically generated and can be either growing or decaying at the time of observation, there is no consensus in the oceanic context. Some believe that oceanic patches are generated by short-lived, spasmodic, extremely powerful turbulence-generating events; at the time of observation, the bulk of these patches are no longer actively turbulent (except at small scales), but are fossil remnants of previously active events (Gibson 1986). An alternative notion is that oceanic patches are persistently in an actively turbulent state, maintained by the energy supplied by environmental sources (Caldwell 1983; Crawford 1986).

Turbulent patches are key to the vertical transport of momentum and species in stably stratified fluids. Patches that do not have a sustained source of turbulent energy decay rapidly, partially destroying the stratification within the patch and creating a horizontal pressure gradient that drives a slow intrusion of the patch. On the other hand, if the turbulence is sustained, for example, by extracting turbulent kinetic energy via mean shear or by artificial agitation, then the intrusion may propagate long distances while the fluid which collapsed into the intrusion is replenished by return currents. As pointed out by Manins (1976), such intrusions are preceded by zero-frequency internal wave modes that travel ahead and remove a part of the energy from the intrusion. Viscous effects may modify these wave modes, and create a slug of fluid pushed ahead of the intrusion (Tritton 1977). For example, when a turbulent patch of vertical height 20 m is generated in a 100 m-thick oceanic thermocline of buoyancy frequency 0.025 rad s^{-1} (De Silva *et al.* 1996), the fastest upstream wave mode will have a velocity of about 0.8 m s^{-1}; in addition, a 15 m-long slug of fluid will be pushed ahead of the intrusion. Under continuous forcing, the upstream motions can propagate long distances and interact with lateral boundaries. An example for this case is the lake destratification work of Lemckert & Imberger (1995), wherein a bubble plume was used to generate isolated turbulent regions in lakes Wungong and Argyle; the resulting laterally confined intrusions were allowed to grow vertically to destratify the lakes. Similar situations can arise in the presence of bottom jets in stratified Karstic lakes (Casamitjana & Roget 1993). As such, studies on isolated turbulent regions in the presence and absence of lateral walls are of interest.

In an attempt at understanding mixing in stratified turbulent patches, Fernando (1988) and De Silva & Fernando (1992) carried out a series of experiments on one-dimensional growth of turbulent patches by vertically oscillating a confined horizontal grid in a linearly stratified fluid (figure 1*a*). Measurements included the growth of the mixed region with time, the internal-wave characteristics at the entrainment interface and other lengthscale relationships. Their results implied that the stratification does not have a significant influence on the growth of the patch, until it grows to a critical height determined by a balance between vertical inertia forces u_H^2/L_H and buoyancy forces N^2L_H or until the bulk Richardson number of the patch $Ri = N^2L_H^2/u_H^2$ reaches a critical value Ri_c. Here N is the buoyancy frequency of the stratification defined by $N^2 = (-g/\rho_0)\,\mathrm{d}\rho/\mathrm{d}z$, g is the acceleration due to gravity, ρ is the density, ρ_0 is a reference density, L_H and u_H are the characteristic integral length and velocity scales of turbulence, respectively. Above Ri_c, the entrainment mechanism intrinsic to non-stratified fluids, i.e. eddy overturning events that engulf non-turbulent fluid, is not possible; entrainment occurs by the breaking of interfacial waves at the entrainment interface owing to local instabilities. As pointed out by De Silva & Fernando (1992) and McGrath, Fernando & Hunt (1997), under these conditions, the local gradient Richardson number in the interfacial zone drops to very small values (despite large Ri), thus triggering local mixing.

Although such one-dimensional patch growth studies are of use in studying the

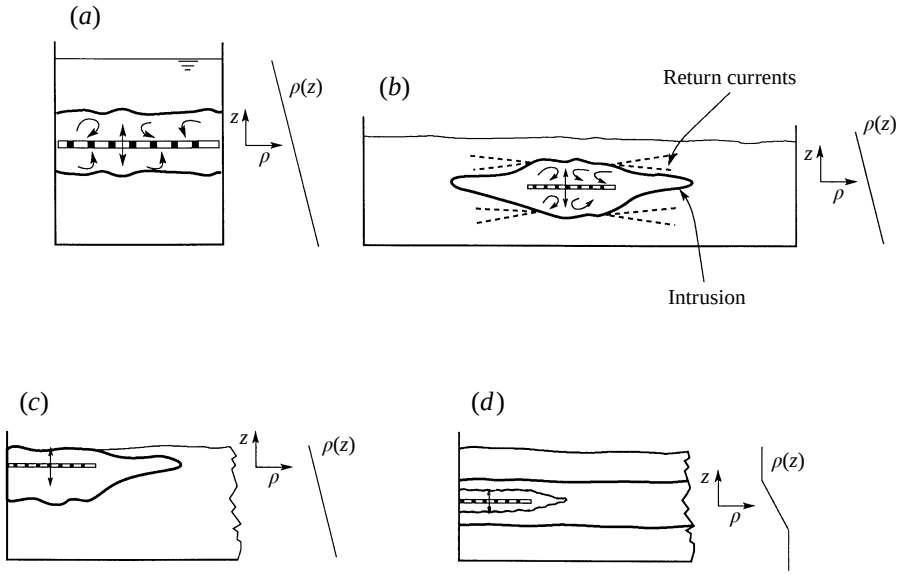

FIGURE 1. Schematic diagrams of the experimental configurations used in different studies. (*a*), (*c*) and (*d*) correspond to the experiments of De Silva & Fernando (1992), Maxworthy & Monismith (1985, 1988) and Brandt & van Heijst (1987), respectively; (*b*) represents the present flow configuration. $\rho(z)$ is the density at a given height z.

inhibition of turbulence by stable stratification, they mimic poorly the long-time evolution of turbulent patches found in nature, which evolve both vertically and horizontally. Their vertical growth is due to entrainment of non-turbulent fluid by the patch turbulence; the predominant horizontal motions take the form of intrusions driven by horizontal pressure gradients developed as a result of localized mixing. The purpose of this paper is to incorporate this additional complexity of lateral developments into our previous one-dimensional experiments. The flow configuration considered is shown in figure 1(*b*), wherein a turbulent region was generated and continuously maintained by a vertically oscillating, horizontal, monoplanar grid. In addition to the vertical growth, the following aspects were studied, namely (i) the initial spreading of the intrusion in which the endwalls of the tank do not play an important role, thus mimicking turbulent patches in natural flows located far from boundaries; and (ii) the development of intrusions subject to the endwall effects, with applications to turbulent patches in confined water bodies such as lakes and estuaries; in such cases, sustained turbulent patches can be generated either naturally, for example, boundary mixing (Caldwell, Brubaker & Neal 1978; Brandt *et al.* 1986), or artificially, for example, using bubble plumes (Lemckert & Imberger 1995). Using detailed flow measurements and scaling arguments, some interesting dynamical features were identified. It is also argued that certain previously held notions on mixed-layer development in confined geometries should be revisited.

The paper is organized as follows. A brief outline of previous work is given in §2. Section 3 deals with the details of the experiment and measurement techniques. The nature of turbulence generated by the source (oscillating grid) in the absence of stratification is described in §4. Sections 5 and 6 present qualitative observations and quantitative measurements pertinent to stratified experiments. A summary of the results is given in §7 and the paper concludes with a discussion in §8 on the geophysical applications of the results.

2. Outline of previous work

Maxworthy & Monismith (1985, 1988) and Brandt & van Heijst (1987) have reported laboratory studies with similarities to the present work. In the former, a linearly stratified fluid was agitated by a horizontal grid placed near the surface of a water column (figure 1*c*), while in the latter study the grid was placed in the centre of a linearly stratified thermocline sandwiched between two homogeneous layers (figure 1*d*). Both of these experiments were designed to simulate local boundary mixing; hence, the grid was located near a corner of the tank. The grid oscillations generated a turbulent mixed region, which collapsed to form a horizontally spreading intrusion. Both studies revealed that the initial spreading of the intrusion takes place at a constant velocity. Maxworthy & Monismith (1985) found $c \propto (fN)^{0.5}$ whereas Brandt & van Heijst (1987) reported $c \propto (fN)^{0.7}$; here f is the frequency of the grid oscillations (in Hz). After some time the intrusion nose was found to decelerate drastically, but eventually it reached the endwalls. Maxworthy & Monismith (1985) attributed this behaviour to the reflection of forward (upstream) propagating internal wave modes at the endwall. Brandt & van Heijst (1987), however, suggested that the lateral (sidewall) blocking of two-dimensional 'pancake' vortices, formed during mixed-region collapse, may cause this deceleration. In this paper, we will show that the arrival of a slug of fluid pushed ahead of the intrusion at the confining walls is the major cause of the deceleration. Another variant observed in the experiments of Brandt & van Heijst (1987) is the formation of breaking Kelvin–Helmholtz billows at the lower edge of the patch, thus making the flow asymmetric about the patch centreline.

Maxworthy & Monismith (1985) identified three phases of evolution: the 'initial' phase consisting of the vertical growth of the patch, the 'spreading' phase of the intrusion with the vertical patch thickness approximately constant and then the 'final growth' phase where the blocked intrusion and the patch grow vertically in unison. They proposed that the growth law for this final phase should be similar to the one-dimensional growth of the patch without lateral spreading, but in the present study we will show (using detailed flow visualization, measurements and a simple entrainment model) that the two cases are fundamentally different.

3. The experiment

3.1. *Apparatus*

A schematic of the experimental apparatus, the dimensions and the coordinate system used are given in figure 2. The test cell is a rectangular Plexiglas tank, with reinforced sides to minimize optical distortions, thus enabling the use of a laser-Doppler velocimeter (LDV). The tank was set up on a horizontal steel table, which also supports the platform for the grid-oscillating mechanism. The grid was driven by a standard slider–crank mechanism; by changing the eccentricity of the crank wheel, a range of strokes, $0.4 < S < 1.5$ cm, could be obtained. In most of our experiments $S = 0.85$ cm was used. The grid-oscillation frequency was continuously monitored using an optical stroboscope of specified accuracy $\pm 0.3\,\%$. The mesh size of the grid was $M = 4.76$ cm, and it was made out of 1×1 cm^2 Plexiglas bars. The diameter of the suspension rods (0.5 cm) supporting the grid was small enough to prevent appreciable mixing around them. The absence of such mixing was verified using shadowgraph observations. The steel table carrying the experimental set-up was placed under another independent frame that supports the instrument carriage and lighting fixtures for flow visualization.

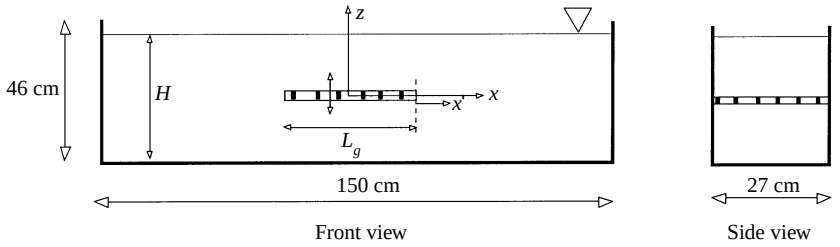

FIGURE 2. Schematic views of the experimental apparatus. The coordinate system used is also shown. x' is the horizontal distance measured from the edge of the grid, while x is that measured from the mid-point of the grid. L_g is the length of the grid.

A supplementary set of experiments was carried out using a horizontal cylinder, fitted with roughness elements (cross-section 1×1 cm, height 1.2 cm and separation 2.5 cm), that makes torsional oscillations. The cylinder was driven by a stepper-motor, programmed to make oscillations of amplitude ($\theta = 3\pi/2$ rad) and frequency $4 < f < 6$ Hz. The aim of this experiment was to investigate whether the results in oscillating-grid experiments had been contaminated by the edge-effects of the grid, for instance, by the vortex formation at the free edge of the grid (as observed by Maxworthy & Monismith 1988). Both oscillating grid and oscillating cylinder experiments showed the same growth behaviour, indicating the absence of any unwarranted endwall effects.

3.2. *Setting up the experiment*

Two types of experiments were performed. In the first set, the grid was oscillated in homogeneous water and the r.m.s. horizontal (u_H) and vertical (w_H) turbulent velocities were measured using a standard single-component LDV. Experiments of the second type were performed in linearly stratified fluids. The tank was filled with a linearly stratified salt solution using the two-tank technique, and the grid mid-plane was at the mid-depth of the water column. The total depth of the water column $2H$ was approximately 30 cm, and the variation from one experiment to another was less than 2 cm. In most experiments salinity stratification was used; in experiments with LDV measurements, a salt–alcohol mixture was used to obtain a uniform refractive-index to avoid problems associated with refractive-index fluctuations (McDougall 1979). The stratification procedure for both cases was the same except that, in the latter case, an aqueous solution of absolute ethyl alcohol (200 proof) having the same refractive index as the salt solution was used in the 'light-water' tank. Since, at low and moderate concentrations, salt and alcohol solutions mix linearly with regard to refractive indices, the mixture emanating from the stratifying system had a constant refractive index; for further details, see Hannoun, Fernando & List (1988).

The grid was placed either at the middle or at the end of the tank. In salt experiments, the vertical salinity distribution was measured using two techniques, i.e. either by using a vertically traversing, calibrated, four-electrode microscale conductivity probe (Head 1983) or by measuring the salinity of samples drawn from different depths using a refractometer. They agreed within $\pm 5\%$. In the salt–alcohol experiments, the density distribution was obtained by vertically traversing a conductivity probe, but the calibration procedure had to be modified to account for the presence of alcohol, as in Perera, Fernando & Boyer (1994).

3.3. *Experimental procedure*

The parameter ranges used for the frequency of grid oscillations (f) and the buoyancy frequency (N) were: $3 < f < 5$ Hz, $0.3 < N < 1.5$ rad s^{-1} and $12.5 < f/N < 90$. The experiments were started by switching on the oscillating mechanism at time $t = 0$. The turbulent region first grew vertically and then collapsed to form a horizontal intrusion at the mid-plane of the grid. Simultaneously, return currents were set up at the edges of the patch to provide make-up fluid. The turbulent region, the intrusion and the return currents were monitored and videotaped using such flow-visualization techniques as shadowgraphs, dye lines, Kalliroscope fluid and neutrally buoyant particles. The flow evolution was videotaped, and the image frames were analysed by mapping the light intensity contours to locate the boundaries of the patch (using digital image processing).

In the dye-line technique, potassium permanganate and Nigrosine crystals were dropped into the fluid to produce columnar dye-lines, as in Manins (1976). Their use, however, was limited to short observational times because of the fading of their appearance following distortions; this problem was alleviated by using dye strings, which were made by soaking thin cotton strings ($\simeq 0.2$ cm diameter) in fluorescent dye solutions and then drying them. The illumination in the (x, z)-plane was provided by a powerful thin sheet of light. A vertical dye string was located at the edge of the grid so that it responded only to the collapsed fluid ejected out of the patch, but not to the slug of fluid that is pushed ahead of the intrusion (see § 5). There was concern that the string itself may cause a blocking influence on the intrusion. To verify this, the speed of the intrusion was measured, in identical experiments, using dye strings and Nigrosine dye lines; no appreciable difference could be observed. In some salt–alcohol experiments, bacteria-stabilized Kalliroscope concentrate was introduced; illumination with a vertical sheet of light produced striking visual images in regions where velocity shear was present. In some experiments, neutrally buoyant tracer particles were added to the test cell, and streak photography was used to estimate the fluid velocity.

The evolution of the density field was monitored using a shooting microscale conductivity probe. The probe was mounted on a stepper-motor-driven, computer-controlled carriage that could be plunged with speeds up to 50 cm s^{-1}. The r.m.s. velocity and buoyancy fluctuation measurements were made along the x- and z-axes; a single-component LDV and a micro-scale conductivity probe, respectively, were used. The output (analogue) signals from the conductivity probes and the LDV were sampled at 400 Hz and 200 Hz, respectively.

4. Measurements in homogeneous water

A large number of previous experiments in confined geometries (as in figure 1(*a*)) have delineated the nature of turbulence induced by oscillating grids (for a review, see Hopfinger & Linden 1982). It is established that the r.m.s. horizontal u_H and vertical w_H velocities and the integral lengthscale L_H (subscript H is used to denote the measurements in homogeneous fluids) are given by

$$u_H = B_1 S^{3/2} M^{1/2} f z^{-1}, \tag{1}$$

$$w_H = B_2 S^{3/2} M^{1/2} f z^{-1}, \tag{2}$$

$$L_H = B_3 z, \tag{3}$$

where B_1, B_2 and B_3 are constants that depend only on grid parameters, M is the grid mesh size, f is the oscillating frequency (in Hz) and z is the distance measured from a

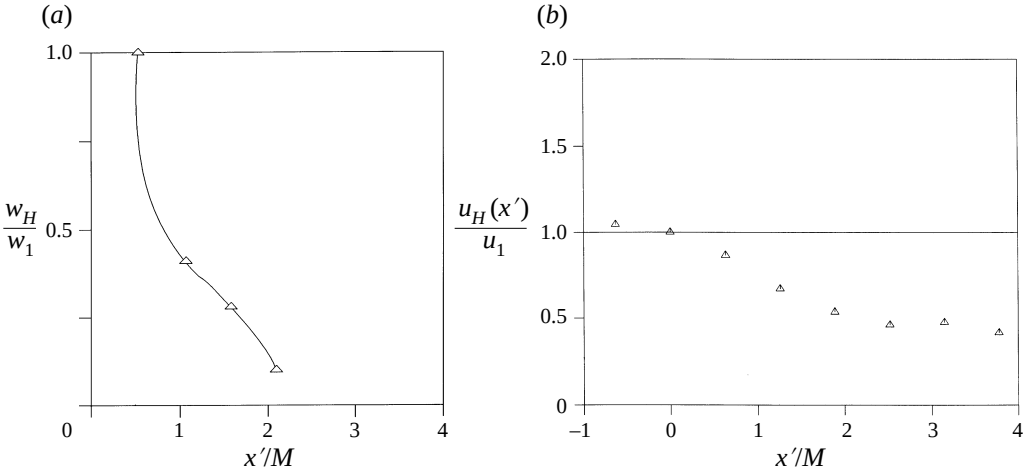

FIGURE 3. (*a*) The spatial decay of normalized r.m.s. vertical velocity w_H with normalized horizontal distance x' measured from the edge of the grid. The grid oscillating frequency was 3 Hz; w_1 represents the velocity at $x' = \frac{1}{2}M$. $K = 2.38$ cm^2 s^{-1} and $S = 1.2$ cm. Data were taken under steady conditions. (*b*) The decay of normalized r.m.s. horizontal velocity u_H with normalized horizontal distance x' measured from the edge of the grid at a distance 7.8 cm below the grid plane. The grid oscillating frequency was 3 Hz: u_1 represents the velocity at $x' = 0$. $K = 2.38$ cm^2 s^{-1} and $S = 1.2$ cm. Data were taken under steady conditions.

virtual origin (which is located close to the mid-plane of grid oscillations). Long (1978) argued that the oscillating-grid turbulence at high Reynolds numbers can be represented by a single parameter called grid 'action', defined as

$$K = u_H z, \tag{4}$$

and, from (1), it appears that $K = B_1 S^{3/2} M^{1/2} f$. It was not clear, however, whether (1)–(4) are applicable to the configuration used in the present experiments; hence, velocity measurements were carried out using the experimental configuration shown in figure 2. The range of the parameters covered was 0.7 cm^2 s$^{-1} < K < 1.3$ cm^2 s^{-1}. The results confirmed that the variation of u_H, w_H and L_H can still be represented by (1)–(3) with $B_1 \simeq 0.15$, $B_2 \simeq 0.2$ and $B_3 \simeq 0.1$; details of these measurements can be found in De Silva (1991).

In addition to the measurements above and below the grid, the decay of w_H and u_H along the horizontal axis x' (see the definition figure 1*b*) was also measured. The purpose of these measurements was to ensure no anomalous flow structures are formed at the edge of the grid, as conjectured by Maxworthy & Monismith (1988). The results are shown in figure 3(*a*, *b*); the velocities here are normalized by their values at $x' = \frac{1}{2}M$ and $x' = 0$, respectively. Note the rapid, monotonic decay, which indicates the absence of grid-forcing effects in the lateral direction over the edge of the grid.

5. Qualitative observations

Videotapes and photographs taken during the experiments were scrutinized to study qualitative aspects of flow evolution. Figures 4(*a*)–4(*i*) show schematics and figures 5(*a*)–5(*i*) show photographs of such events. Soon after the onset of grid oscillations, a mixed region surrounds the grid, growing mostly in the vertical direction (figures 4*a* and 5*a*); this is the 'initial growth' regime, which was similar to that reported by

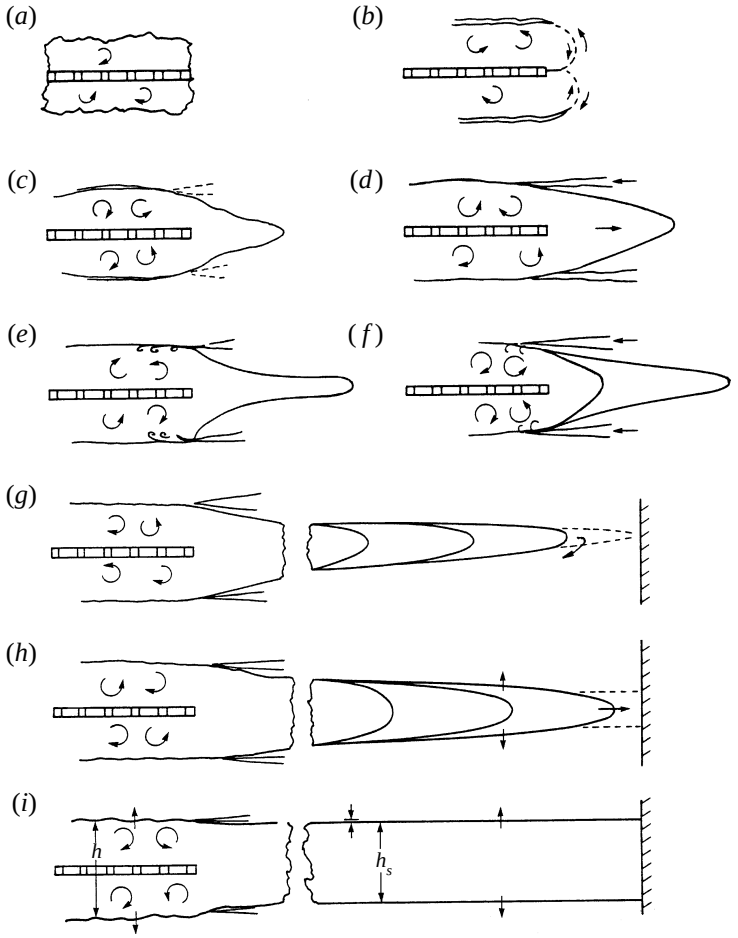

FIGURE 4. Schematic diagrams that illustrate a possible evolution scenario. (*a*) Initial vertical growth of the mixed layer. (*b*) Mixed region is on the verge of gravitational collapse. (*c*) Spreading of the intrusion at the equilibrium density level of the mixed fluid (with collapse, a reduction in the average patch thickness can be observed. (*d*) Return currents are set up to replenish the lost fluid. (*e*) Fluid from the return currents are entrained into the patch; the stratification within the patch is enhanced thereby reducing the volume flux fed into the intrusions (*f*) Stratification within the patch is reduced again and the velocity of the intrusion is increased. (*g*) The slug of fluid pushed ahead of the intrusion reaches the endwalls of the tank and the speed of the intrusion is decreased. (*h*) The upstream slug of fluid is pushed against the endwall and the collapsed fluid starts accumulating in the side arm. (*i*) The side arm is filled with the collapsed fluid, and both turbulent patch and the side arm grow in the vertical direction.

Fernando (1988). At a non-dimensional time $Nt \sim 4$, the vertical growth stops and well-defined interfacial layers (figure 4*b*) separating the turbulent and non-turbulent regions appear. At about $Nt \simeq 5$–8, the mixed layer collapses and ejects mixed fluid horizontally to form intrusions propagating along their equilibrium density-level $z = 0$ (figures 4*c* and 5*b*). At any $z > 0$ ($z < 0$), the density within the patch is greater (lower) than the density of the ambient fluid, and the horizontal pressure gradient generated owing to the resulting hydrostatic-pressure imbalance causes the ejection of fluid out of the patch.

Once the intrusion starts spreading, the average vertical thickness of the patch

reduces slightly. To replenish ejected fluid, return currents are generated at the edges of the patch (figures 4*d* and 5*c*). The intrusion is symmetric from the side-view, and no evidence was found for the presence of Kelvin–Helmholtz instabilities at the edges of the intrusion. Dye injected into the mixed patch shows that large, flat, pancake-like eddies are present near the nose of the intrusion but they are not typically blocked by the sidewalls. These two observations are at variance with those of Brandt & van Heijst (1987). The thickness of the return currents grows with x'; this can be construed as a case of selective withdrawal wherein the fluid is absorbed into the patch through thin slits at the edges of the patch. The return currents are subjected to entrainment by the turbulent eddies within the patch. The entrainment begins at the edge of the patch and is usually completed before the return currents reach the centre of the patch (figures 4*e*,*f* and 5*d*).

With the arrival of return currents, the patch expands to its original size. The incoming fluid at the upper edge is lighter (and the lower edge is denser) than the rest of the turbulent fluid and, hence, there is a tendency for the patch to restratify partially. For instance, for $z > 0$, the lighter fluid from the return current mixes with the heavier fluid from the patch, thus temporarily generating a stable density gradient, which is later destroyed by the turbulence. Consequently, the horizontal pressure gradient that forces fluid out of the patch into the intrusion diminishes, as does the volume flow-rate of collapsed fluid. (The reduction in the vertical size of the patch may also be a contributing factor for the reduction in the intrusion speed.) The fluid already in the intrusion continues to spread, but since a lesser amount of fluid now enters the intrusion, a neck appears outside the patch, as shown in figure 4(*e*).

As the volume-flow rate into the intrusion reduces, the inflow by the return currents also decreases. This trend is reversed when continued stirring within the patch destroys the newly formed stratification, thereby reinstating the horizontal pressure gradient. The fluid velocity within the intrusion increases again, thus leading to a pulsating flow. The throbbing nature of the flow is evident from the dye-line flow visualization; a sudden increase of velocity tends to detach high concentrations of dye, as depicted in figures 4(*g*) and 4(*h*) and as evident from figures 5(*e*) and 5(*f*).

The succession of events, namely, the collapse of the patch fluid, the replenishment of 'lost' fluid by the return currents, the restratification within the patch and associated reduction of the fluid velocity within the intrusion, the breakdown of the stratification, and the increase of the fluid velocity, continues, thus leading to the pulsating flow within the intrusion. Peyret (1976), in a numerical study on a horizontal jet discharging into a stratified environment, has also observed pulsations of the flow velocity; this was attributed to the presence of eddies. As pointed out by a referee, another possible contribution to this unsteady flow is the background internal wave field that can distort the patch and intrusion, thus changing the volume flow rate into the intrusion periodically. This aspect will be further addressed in §6.3.

Another noteworthy observation is the upstream blocking of the intrusion. Dye lines placed ahead of the intrusion clearly demonstrated that a wedge-shaped slug of fluid is pushed ahead of the intrusion (figure 5*g*). As the nose of this slug reaches the endwalls of the tank, upstream blocking occurs, although the intrusion nose has not yet reached the endwalls. The intrusion, however, continues to spread by forcing the slug against the endwalls ('blocked regime'). Detailed observations reveal that the spreading under such conditions can occur by splitting the slug and forcing its fluid to flow as return currents (figures 4*g* and 4*h*). During this process, an adverse pressure gradient is developed and the intrusion decelerates. As more and more collapsed fluid is fed into the intrusion, the thickness of the intrusion increases (figure 4*h*); the

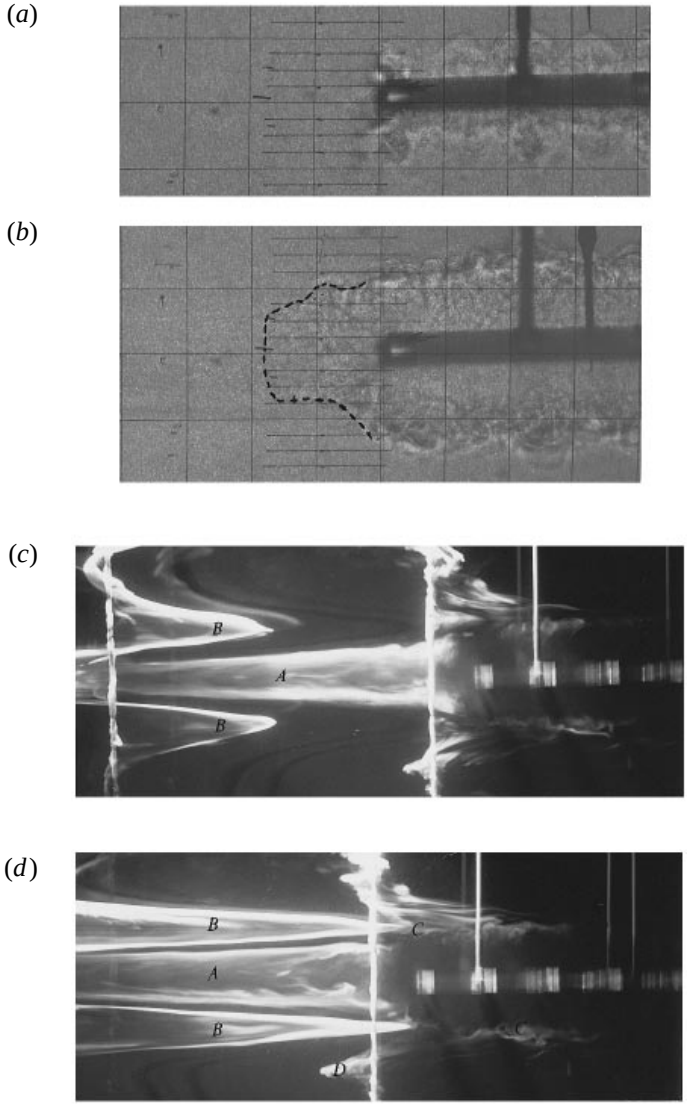

FIGURE 5(*a–d*). For caption see facing page.

horizontal pressure gradient driving the intrusion decreases and a sluggish evolution of the system can be observed. With time, the mixed fluid fills up the region between the patch and the walls (henceforth called the 'side arm') (figures 4*i* and 5*h*). Under these conditions, the intrusion is 'fully blocked' and the nose of the intrusion has reached the endwalls.

The vertical size of the patch remains approximately constant until the intrusion is blocked by the endwalls, and then starts to grow slowly ('transient subsequent growth'). Once the side arms is filled with the mixed fluid, both the patch and the side arm grow in the vertical direction at approximately the same rate ('final subsequent growth'). In this latter regime, the vertical thicknesses of the path h and the side arm h_s appear to be the same on a shadowgraph (figures 4*i* and 5*i*), but detailed observations with proper illumination indicate that h_s is slightly less than h, and that

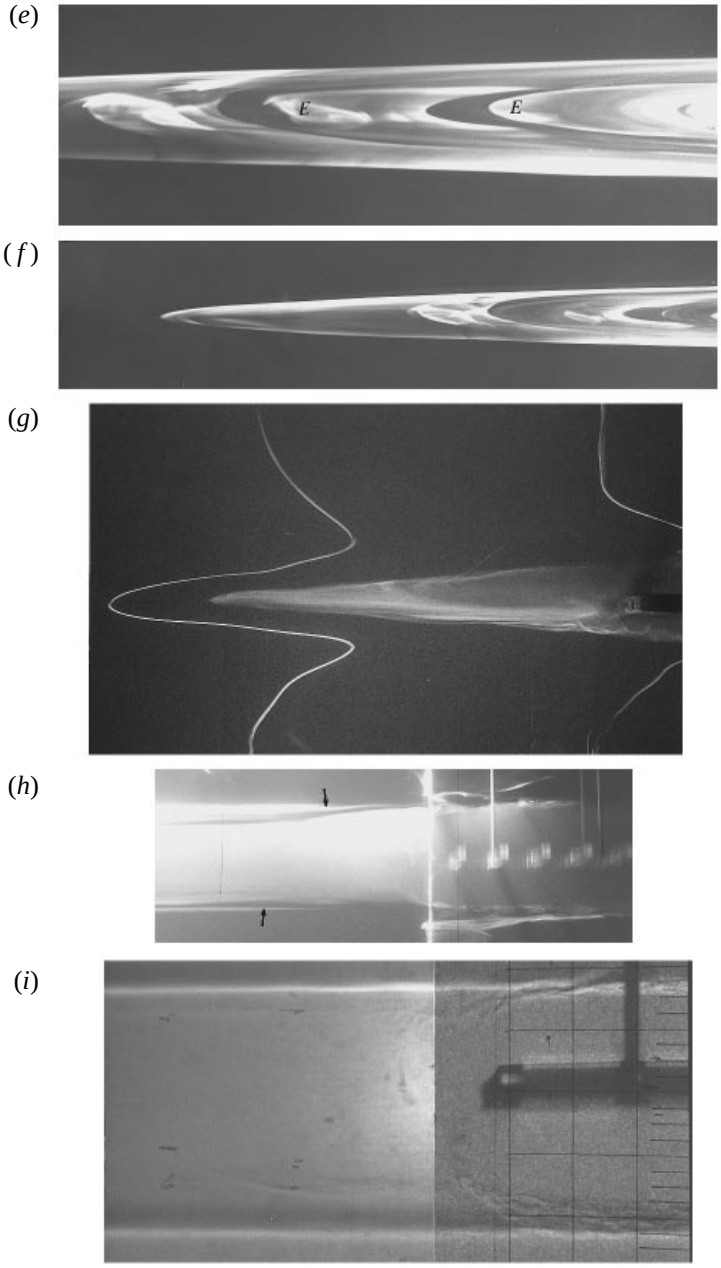

FIGURE 5. Photographs depicting various features of the evolution of the patch. (*a*, *b*) The initial vertical growth (at $Nt \simeq 2$) and collapse of the patch (at $Nt \simeq 10$), respectively. The boundary of the intrusion is marked with a dashed line. (*c*, *d*) The dye-line flow visualization of the intrusion and the return currents: *A*, intrusion; *B*, return currents; *C*, entrainment of the fluid from the return currents into the intrusion; *D*, dye movement due to initial transient velocity field. (*e*, *f*) The features at different locations of the intrusion. Note the appearance of successive tongue-like features (*E*). Unlike the observations of Brandt & van Heijst (1987), the intrusion is symmetric and no appreciable Kelvin–Helmholtz instabilities can be observed at the lower boundary. (*e*) The central part of the intrusion and (*f*) the nose. This photo was previously published in the cover page of *EOS* **69** (12), 1988. (*g*) The upstream influence in which a slug of fluid is pushed ahead of the intrusion. The fluid in the upstream starts moving before the arrival of the intrusion as indicated by the dye line distortions. (*h*, *i*) These are pertinent to the subsequent growth. Note the presence of thin return currents (marked by arrows) in (*h*). The shadowgraph view of a similar flow situation is given in (*i*); because the flow structure is horizontally averaged, some details such as return currents revealed in (*h*) are not evident here.

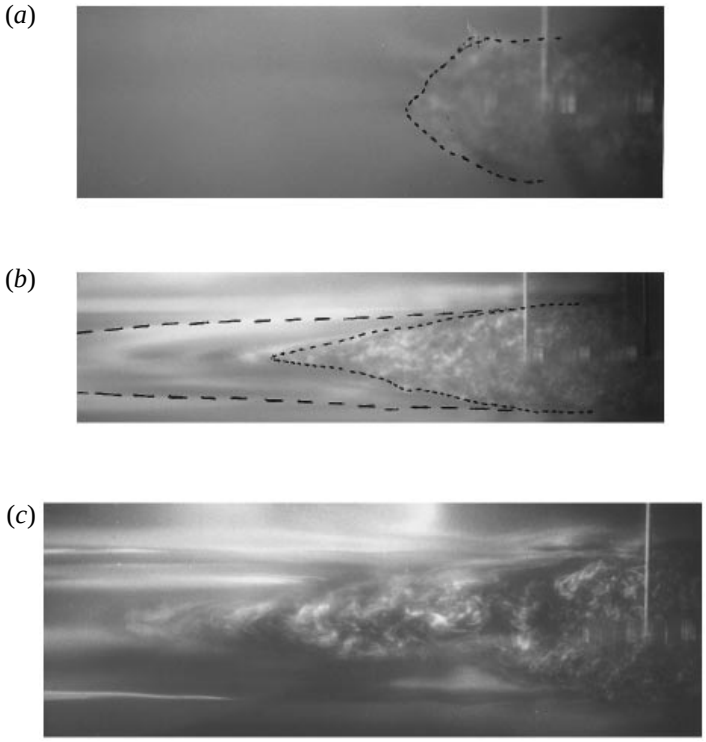

FIGURE 6. The growth of the turbulent patch, as visualized using Kalliroscope fluids. (*a*) The beginning of the collapse. ---, the boundary of the turbulent region. (*b*) During the spreading of the intrusion. – – –, the 'turbulent core'; ———, the boundary of the intrusion. (*c*) The flow structure during the final growth. In cases (*b*) and (*c*), gradual disappearance of the active turbulent core along the x-axis can be seen. The experimental conditions are $f/N = 36$ and $S = 0.85$ cm.

the upper and the lower boundaries of the side arm have a slight inclination to the horizontal. As is evident from figures 4(*h*) and 5(*h*), the movement of dye lines placed near the far end of the tank show the presence of thin return currents even during the 'final subsequent growth'.

It is noted that dominant motions in the experiment tank are confined to the patch, the intrusion and return currents. Motions in the rest of the fluid essentially consist of weak internal waves generated during the collapse (e.g. Wu 1969). As soon as the return currents were initiated, substantial fluid motions were detected over the whole tank, but the motion away from the fluid layer containing the patch decayed rapidly; thus leaving a motion field confined to the surrounding of the patch (i.e. the intrusion and return currents, figure 4*d*). According to Pao & Kao (1974), such transients are typical during the set-up of selective withdrawal in stratified fluids.

Finally, it is worth noting some of the key observations made with Kalliroscope fluids. Figure 6 shows photographs taken at different stages of the intrusion formation. Note the images produced by the local fluctuating shear of turbulence, which show the existence of a 'turbulent core' within the intrusion. Along the intrusion the r.m.s. velocity and potential energy fluctuations decay gradually, thereby reducing the vertical thickness of the turbulent core.

6. Quantitative observations

6.1. *Thickness of the collapsing patch*

As the turbulent patch grows vertically, according to (4) the turbulent velocity scale decreases as $u \sim K/r$, where r is the half-patch thickness. Meanwhile, the buoyancy forces on turbulent eddies of scale r increase as $N^2 r$. Hence the vertical growth of the patch is arrested by the stratification when the vertical inertia forces u^2/r of the eddies balance the buoyancy force $N^2 r$ at a patch thickness of $r_c \sim (K/N)^{1/2}$. The patch-thickness measurements made using instantaneous density profiles taken by the shooting conductivity probe are shown in figure 7, as a plot of r_c versus $(K/N)^{1/2}$. These results together with $L_H \simeq 0.1\, r_c$, give

$$r_c \simeq 4.7\ (K/N)^{1/2}, \tag{5a}$$

$$Ri = \frac{N^2 L_H^2}{w_H^2} \simeq 2.7, \tag{5b}$$

$$Fr = \frac{w_H}{N L_H} \simeq 0.60, \tag{5c}$$

where Ri and Fr, respectively, are the Richardson and Froude numbers of patch turbulence. This particular Fr compares well with the critical Froude number ($Fr_c = 0.63$) at which the growth of turbulent lengthscales is inhibited by the stratification (Stillinger, Helland & Van Atta 1983). (However, Fr_c evaluated from many different laboratory experiments shows a wide variation. By analysing a number of laboratory studies, Hopfinger (1987) concluded that Fr_c should be of order 1. Further discussions can be found in Roberts & Matthews (1986). This also implies that the vertical scale at the collapse should be proportional to the Ozmidov (1965) scale $L_R = (\varepsilon/N^3)^{1/2}$. By assuming $\varepsilon \simeq w_H^3/l$ and using 5(a) we obtain $r_c \simeq 21 L_R$ or $l \simeq 2.1 L_R$.)

Upon reaching the maximum height (5a), the mixed fluid in the patch slumps (or collapses) to form an intrusion. To quantify this process, the times t_{c1} and t_{c2} required for the intrusion nose to arrive at $x' = 1.25$ cm and $x' = 2.5$ cm (cf. figure 2), respectively, were measured using video images. These collapse (or intrusive) times t_{c1} and t_{c2} versus $1/N$ data, shown in figure 8, indicate they are proportional to each other with $Nt_{c1} \simeq 5$ and $Nt_{c2} \simeq 13$.

6.2. *Spreading of the intrusion*

The time growth of the intrusion was measured as discussed in §3.3. The non-dimensional mean position of the intrusion nose $x_n'/(K/N)^{1/2}$ as a function of the non-dimensional time Nt so obtained is shown in figure 9; it contains data from two different grid positions, namely, located at either the middle or at the end of the tank. Note that initially the nose location x_n' is proportional to t, but after some time the propagation speed becomes slower, indicating upstream blocking. As expected, the upstream influence is felt much sooner when the grid is placed at the middle of the tank. To calculate the average intrusion speed c in the 'initial' (linear) spreading regime $x_n' - t$ data were least-square fitted with a straight line; initially, only the first five data points were included, and then the number was gradually increased until the correlation coefficient dropped below 90%. The data taken beyond this point, say $x_n' = x_b$, were considered to be in the 'blocked' regime, whence c was calculated using a third-order spline-fit to $x_n' - t$ data. The distance between the endwall and $x' = x_b$ was considered as the length of the slug λ that is pushed ahead of the intrusion.

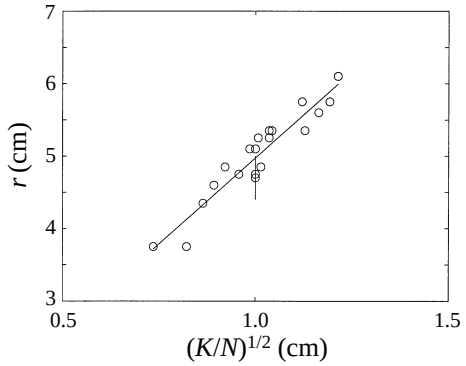

FIGURE 7. A plot of non-dimensional half thickness of the turbulent patch at the onset of collapse r_c vs. $(K/N)^{1/2}$. The parameter range is $15.4 < f/N < 34$ and $S = 0.85$.

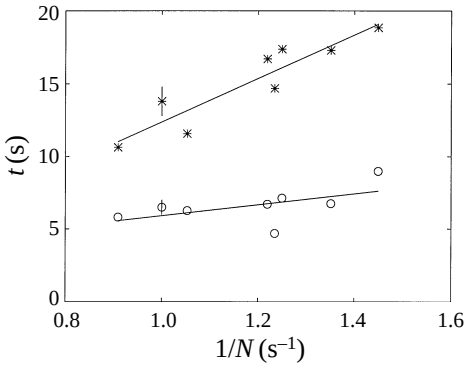

FIGURE 8. A plot of non-dimensional collapse times vs. the inverse buoyancy frequency. ○, t_{c1} and ✳, t_{c2}; $S = 0.85$ cm and $30 < f/N < 88$.

Results of figure 9 show that in the 'initial' spreading regime (i.e. $x_n' < x_b$), the intrusion speed satisfies the following relationships

$$c \simeq 0.71\ (KN)^{1/2}, \tag{6a}$$

or

$$Fr_i = \frac{c}{Nr_c} \simeq 0.15, \tag{6b}$$

where Fr_i is the internal Froude number of the intrusion. To check whether 6(a) depends on such external parameters as the width W and length L of the tank or the water depth $2H$, a series of experiments was carried out by varying W/L and W/H; no systematic dependencies were observed (the details of these experiments are described in De Silva 1991).

In addition, experiments were performed to investigate the effect of the grid length L_g (or the ratio L_g/L) on the intrusion propagation speed. The same tank and two grids of dimensions 60×30 cm^2 and 30×30 cm^2 were used. All other parameters of the grids, as well as the oscillating frequency and the buoyancy frequency, were kept the same. The data so obtained were very useful in delineating the mechanism controlling the volume transport by the intrusion. Maxworthy & Monismith (1988) argued that the intrusion propagation speed is set by the rate of turbulent entrainment into the patch (through upper and lower turbulent/non-turbulent interfaces) over the length of the grid. They further assumed that the rate of entrainment in the presence of the intrusion

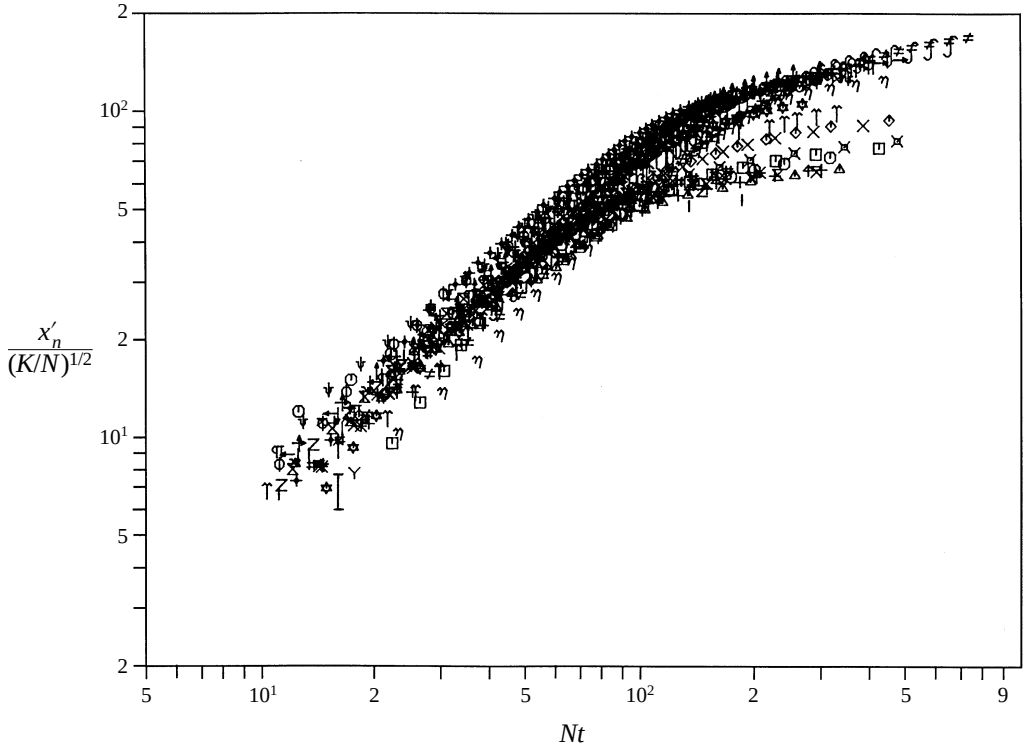

FIGURE 9. A plot of normalized position of the intrusion nose vs. non-dimensionalized time. Experimental data for two grid positions are given. The data with the shorter linear range correspond to the case where the grid was in the middle of the tank. $S = 0.85$ cm and $19.6 < f/N < 31.1$.

is the same as that of the one-dimensional patch growth case where intrusions are absent. Figure 10 shows $x'_n - t$ measurements of a pair of experiments. It is clear that the intrusion speed is not dependent on L_g/L, a result at variance with the proposal of Maxworthy & Monismith (1988); according to their proposal, the total volume of fluid entrained into the patch with the longer grid should have been twice as much as that of the shorter grid, a difference that should be reflected in the nose propagation speed. As will be discussed later, the volume flux into the patch is dominated by the return currents at the edges of the patch (figure 5(*c*) and 5(*d*) rather than the entrainment contribution, and this is why the intrusion speed is independent of grid length.

6.3. *The role of internal waves*

At first glance, the observation $Fr_i = c/Nr_c = \text{constant}$ in the 'initial' spreading regime implies that there is a balance between horizontal inertial forces of the intrusion ($\sim c^2/x'_n$) and the driving horizontal pressure gradient force ($\sim N^2 r_c/x'_n$). If such a balance exists, however, Fr_i should be order one, rather than 0.15 as observed here. The discrepancy suggests that the intrusion dynamics is far more complex than a simple inertia–pressure gradient balance. Below, we will show how the dynamics of low-frequency internal waves excited by the intrusive flow can explain the observed low Fr_i. Then we will discuss how some of the low-frequency waves can be modified by viscous effects to produce a slug of fluid pushed ahead of the intrusion (leading to upstream blocking).

In the present flow configuration, internal waves can be generated owing to two mechanisms, namely, (i) the release of potential energy during the collapse of the patch

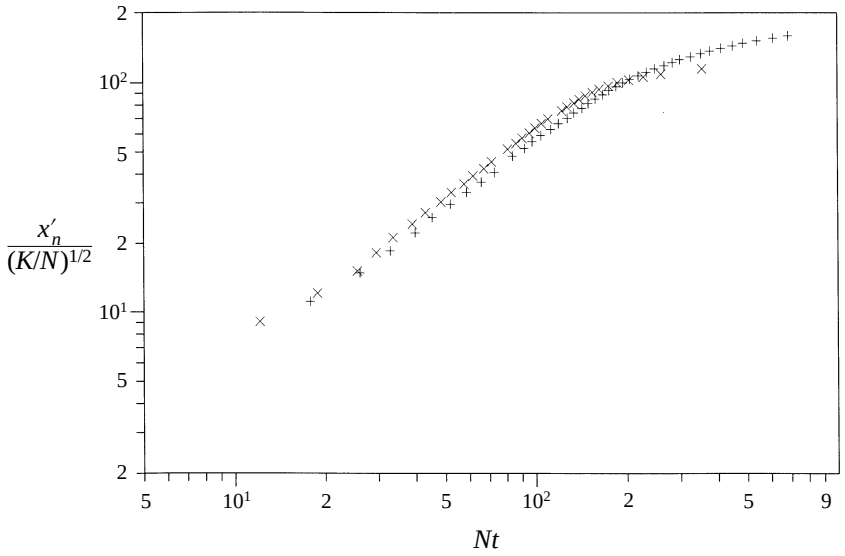

FIGURE 10. The growth of the non-dimensional length of the intrusion with non-dimensional time Nt for two experiments with identical parameters, except the length of the grid; $\times$, $L_g = 60$ cm; $+$, $L_g = 30$ cm. The other parameters $N \simeq 1.01$ rad s^{-1} and $K \simeq 1.51$ cm^2 s^{-1}.

fluid (similar to that described by Wu 1969), and (ii) the forcing imposed on the background stratification by the propagating intrusion. According to Wu (1969), the mechanism (i) is most effective during the initial collapse and it produces waves with frequencies around (0.6–0.8) N. These waves propagate away, carrying energy from the source. Also, they can be reflected at the tank boundaries and can persist in the stratified layer because of their relatively slow decay. Measurements discussed in §6.5, however, indicate that these waves may not be sufficiently energetic to exert a significant impact on the intrusion. It is the waves generated by mechanism (ii) that appear to have a significant influence on intrusion speed, as the following discussion indicates.

Because the upper and lower boundaries of the intrusion are nearly horizontal, the phase surfaces of wave-like disturbances generated by the intrusion are expected to have the same inclination. This implies that the wavenumber vector of these disturbances is nearly vertical, and hence the frequencies ω of internal wave motions, given by the linear theory as $\omega = N\cos\theta$, are near zero; here θ is the inclination of the wavenumber vector to the horizontal. (For example, when an intrusion generated by a patch of $r_c = 5$ cm travels a distance of $x_n' = 50$ cm, the boundaries of the intrusion have an inclination of 5.7° to the horizontal or $\omega = 0.1N$.) Under such conditions, the fluid particles move in nearly horizontal layers, sliding over one another in opposite directions, thus generating strong shear between them. Owing to the lack of restoring buoyancy forces on them, these sliding motions continue, and when $\theta = \pi/2$, the period of the resulting wave field is infinitely large ($\omega = 0$). The observed sliding fluid layers surrounding the intrusion can be considered as signatures of these low-frequency wave modes.

The speed of propagation of zero-frequency internal waves is determined by the wave mode (or the vertical wave number); in the inviscid limit, the mth mode has a group velocity of (Manins 1976)

$$C_m = \frac{NH}{m\pi}, \tag{7}$$

where $2H$ is the depth of the water column. From (7), it is clear that the wave modes satisfying $C_m > c$, or equivalently the wave modes with $m < M$, where

$$M = \text{Integer Part}\left(\frac{NH}{\pi c}\right), \tag{8}$$

propagate faster than the intrusion, thus modifying the upstream flow. These wave modes can carry energy out of the intrusion, thus slowing it down and yielding low Fr_i values as observed above.

A quantitative assessment on the effects of low-frequency internal waves can be made by estimating the energy loss to the upstream propagating waves. Manins (1976) considered the motion of a two-dimensional intrusion in a linearly stratified fluid at its neutrally buoyant level, issued by a source having a volume flow rate q. It was shown that the frontal position x_m of mth mode zero-frequency disturbances propagates according to

$$x_m = \frac{HNt}{m\pi} + 3^{7/3}\frac{\beta_1 H(Nt)^{1/3}}{2m\pi}, \tag{9}$$

where β_1 is a constant of order one. If the confining lateral boundaries are far away, the wave modes having speeds greater than the intrusion speed simply propagate away, carrying energy with them and reducing Fr_i of the intrusion. Using a hydraulic model, Manins (1976) calculated the resulting Fr_i as

$$Fr_i^2 = 1 + \frac{2D}{H} - \sum_{m=1}^{M}\frac{2Fr_i}{m\pi(1 - m\pi\phi_1 Fr_i)}, \tag{10}$$

where D is the thickness of the density transition layer from the ambient linear stratification to the well-mixed intrusion fluid, $\phi_1 = \gamma/H$ is the aspect ratio and t is the thickness of the intrusion.

On the other hand, if the walls are not so far away, the upstream-propagating wave disturbances reflect from the endwalls to self-cancel the forward and reflected waves. Thus, only the wave modes propagating slightly faster than the intrusion, i.e. mode M, can effectively take away energy out of the intrusion. It should also be noted that, although mode M is the slowest, it has the largest amplitude of all upstream modes (Wong & Kao 1970). Calculations based on the hypothesis of wave-mode cancellation during reflection predicts that Fr_i should be determined by (Manins 1976)

$$Fr_i^2 = 2.2 - \frac{2Fr_i}{M\pi(1 - M\pi\phi Fr_i)}. \tag{11}$$

For the present flow configuration with typical values of $N \approx 1$ rad s^{-1} and $H \approx 15$ cm, the fastest propagating wave mode is expected to travel at a speed $C_1 = NH/\pi \approx 4.8$ cm s^{-1}, which reaches the opposite endwall of the tank at a time $(L - L_g)/C_1 \approx 25$ s; here $L = 150$ cm and $L_g = 30$ cm. As this timescale is small compared to that of the intrusion spreading, the wave reflection is expected to play a dominant role in the spreading of the intrusion; hence (11) is the proper choice for estimating Fr_i.

The possible number of upstream propagating disturbances can be evaluated using (8), for typical values of $N \approx 1$ rad s^{-1}, $H \approx 15$ cm and $c \approx 0.6$ cm s^{-1}; as $M = 8$. In addition, using the characteristic values $\gamma \approx r_c = 5$ cm, $H = 15$ cm (or $r_c/H = \phi_1 = 0.33$), it is possible to calculate the Fr_i of the intrusion using (11) as $Fr_i \approx 0.13$. The closeness of this calculated value to the experimental observations (≈ 0.15), indicates that indeed the intrusion motion is governed by the complex dynamics of zero-frequency, forward-propagating internal waves excited by the intrusion itself.

Now we return to discuss possible implications of high-frequency waves generated

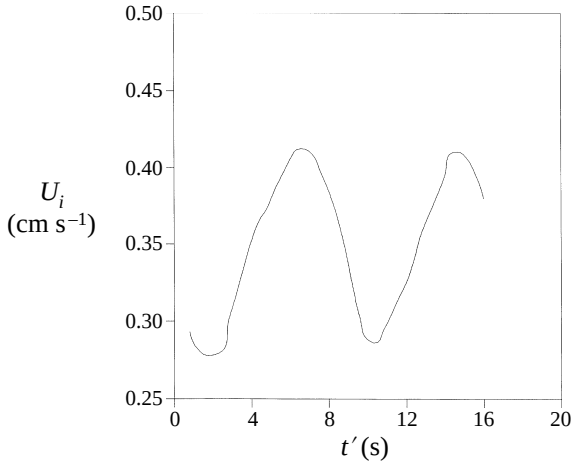

FIGURE 11. Variation of the mean velocity within the intrusion with time t'. The origin t' is arbitrary. The experimental conditions are $K \simeq 0.75$ cm^2 s^{-1}, $N \simeq 1.16$ rad s^{-1}, $S = 1$ cm and $f/N = 12.4$.

by mechanism (i). In § 5, the pulsating nature of the flow within the intrusion (observed qualitatively) was discussed in light of possible periodic destratification and restratification within the patch. To confirm this unsteadiness, the mean velocity U_i within the intrusion was measured using a laser-Doppler velocimeter placed at $x' = 15$ cm and $z = 0$. The results are shown in figure 11 and provide clear support for the existence of pulsations. A referee pointed out that the straining motions of background internal waves (generated by the mechanism (i)) can be a cause for these pulsations. This can be checked by using the velocity trace of figure 11, which has a periodicity of 8 s or $\omega \approx 0.78$ rad s^{-1}; based on $N = 1.16$ rad s^{-1}, the normalized frequency of flow oscillations in the intrusion becomes $\omega/N = 0.6$. Given that this non-dimensional frequency is in the same frequency range $\omega/N \approx (0.6–0.8)$ as the internal waves generated by the patch collapse, one may conclude that background internal waves can indeed play a role in the observed unsteadiness. Further work is necessary to delineate the exact cause of the unsteadiness.

Note that the internal-wave calculations presented above are based on the inviscid assumption. One major manifestation of viscosity in the present flow is the formation of a slug of fluid pushed ahead of the intrusion (figure 5(*g*)). As pointed out by Tritton (1977), in the absence of viscosity, a low Fr_i two-dimensional intrusion can push the entire upstream fluid layer and slide it horizontally through the rest of the fluid (thus exciting low-frequency internal waves). This is because the shear layer between the upstream flow and the background does not permit raising (or lowering) of the upstream fluid to pave the way for the intrusion to debouch; for such vertical deflections of fluid particles to occur, the upstream flow should acquire vorticity, which is not permitted in the inviscid limit. In the presence of viscosity, however, the sharp boundaries between the sliding layers smear out, diffusing vorticity of the shear layer into the upstream fluid column and permitting some of its fluid elements (located at a certain distance) to deflect and flow over the intrusion. Thus, only a slug of fluid, instead of a long column, upstream of the intrusion is pushed ahead. The 'blocked' regime occurs when this upstream slug (or low-frequency wave modes modified by viscosity) reaches the endwall. The measurements of the slug length and comparison of the results with the scaling proposed by Tritton (1977) are given in De Silva (1991).

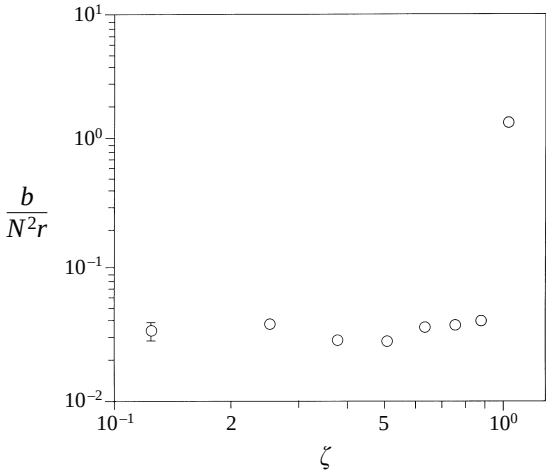

FIGURE 12. Variation of non-dimensional r.m.s. buoyancy fluctuation with non-dimensional distance $\zeta\ (= z/r)$. $S = 0.85$ cm and $f/N = 38$.

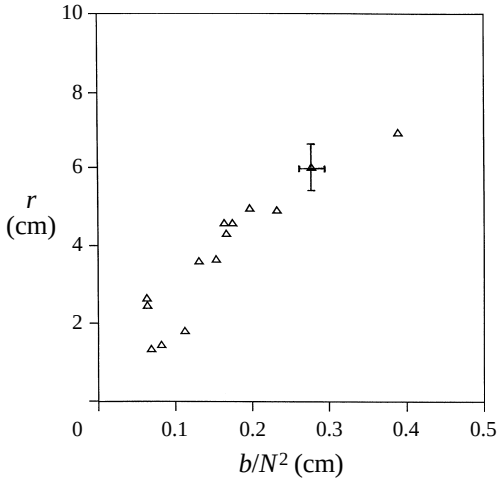

FIGURE 13. A plot of half-patch size r vs. the overturning lengthscale $L_T = b/N^2$. $S = 1$ cm and $14.4 < f/N < 33$.

6.4. *Scales of turbulence within the patch*

Certain key turbulence scales pertinent to the patch, namely, the r.m.s. buoyancy fluctuation, Thorpe overturning lengthscale, maximum Thorpe displacement and the overturning lengthscale were measured and the results are discussed below.

Figure 12 shows the variation of the r.m.s. buoyancy fluctuation b along the vertical centreline of the patch, based on time series measurements at various locations; here $\zeta = z/r$, r is the half-patch thickness and the buoyancy is defined as $b = (\rho_0 - \rho)\, g/\rho_0$. Note that in the bulk of the mixed region, the r.m.s. buoyancy fluctuation tends to be constant indicating uniform mixing of the active scalar over the patch. In the interface, however, b is higher owing to the trapping of interfacial waves. Using the average b in the patch, the overturning lengthscale $L_T = b/N^2$ was calculated, and the results are shown in figure 13 as a plot between L_T and the half-patch thickness; a relation of the forms $L_T \simeq 0.05r$ is clearly evident from the results. Other definitions of the overturning lengthscale are $L_{TS} = 2b/N^2$ (Stillinger *et al.* 1983) and $L_{TG} = 2\sqrt{2b/N^2}$

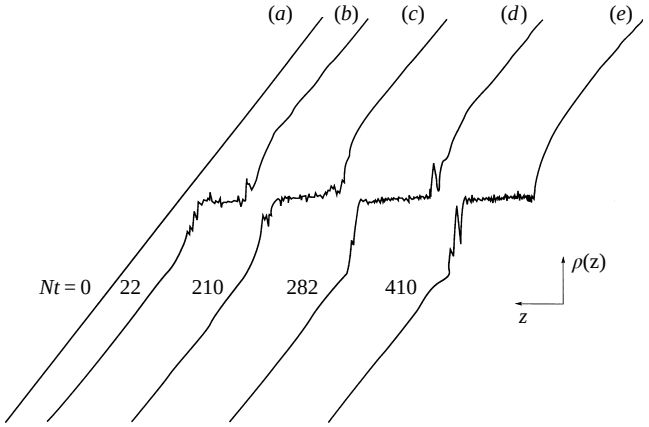

FIGURE 14. Density profiles taken through the patch at different stages of its evolution. Pertinent Nt values are shown. For this experiment $N \simeq 1.0$ rad s^{-1}, $S = 0.85$ cm and $f/N = 80$. The axes are arbitrary.

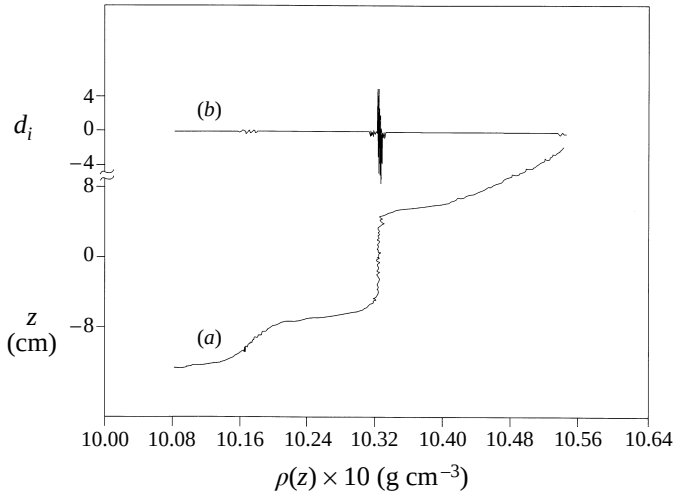

FIGURE 15. (*a*) A density profile taken through the turbulent core in the intrusion. (*b*) The Thorpe displacements corresponding to the density profile in (*a*). $S = 0.85$ cm and $f/N = 31$.

(Gargett, Osborn & Nasmyth 1984). Using $r_c \simeq 10L_H$ and $L_H \simeq 2.1L_R$, where L_R is the Ozmidov scale, we obtain, $L_{TG}/L_R \simeq 3.0$. It is interesting to note that the laboratory measurements of Stillinger *et al.* (1983) in a water channel show $L_{TG}/L_R \simeq 2.0$, whereas oceanic field measurements of Gargett *et al.* (1984) indicate $L_{TG}/L_R \simeq 2.2$.

The Thorpe lengthscale and the maximum Thorpe displacement are often used as convenient measures of the scale of turbulence in stratified fluids (Dillon 1984; De Silva & Fernando 1992). These lengthscales are calculated using measured instantaneous density profiles through the patch (§3.3); such profiles contain small-scale overturns, and are rearranged using a bubble-sort algorithm to obtain statically stable (Thorpe-ordered) profiles. The vertical distances that fluid particles had to be displaced to construct the Thorpe profiles are known as the Thorpe displacements, d_i (Thorpe 1977). The maximum absolute value of Thorpe displacements is defined as the maximum Thorpe displacement d_{max} while the r.m.s. of Thorpe displacements is defined as the Thorpe lengthscale L_{Th}. Figure 14 shows a sequence of vertical density profiles

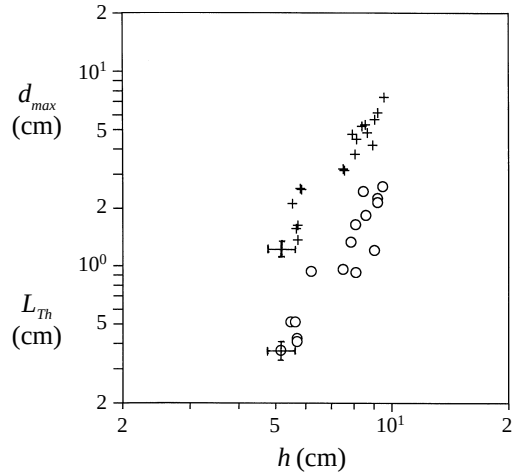

FIGURE 16. Variation of the Thorpe lengthscale L_{Th} and the maximum Thorpe displacement d_{max} with the vertical thickness of the path h. $S = 0.85$ cm and $23 < f/N < 62$.

taken through the patch at various stages of evolution. Note the presence of small-scale overturning motions within the patch and a strong activity of trapped internal waves in the interface between turbulent and stratified layers. Visual observations show that intermittent breaking of trapped waves leads to strong density and velocity fluctuations at the interface. Figure 15 shows a typical density profile and the resulting Thorpe displacements; note that the Thorpe displacements are found only within the patch and in the turbulent core of the intrusion (figure 6*b*).

Figure 16 shows the variation of L_{Th} and d_{max} measured within the patch with the physical thickness h of the collapsing patch taken at $Nt > 100$. Note that both L_{Th} and d_{max} increase with the patch size. Regression analysis shows that $L_{Th} \propto h^{2.7}$ and $d_{max} \propto h^{2.7}$. These results are in general agreement with the measurements taken in non-collapsing patches by De Silva & Fernando (1992), for the ranges of patch sizes considered, indicating the similarity of the size of overturning motions, irrespective of whether the patch is collapsing or not. Figure 17 shows the measurements taken along the intrusion at $Nt > 400$, within which the 'turbulence core' decays as depicted in figures 6(*b*) and 6(*c*). The best-fit lines to this somewhat scattered data indicate power laws of the form $L_{Th} \propto \delta^{2.2}$ and $d_{max} \propto \delta^{2.2}$, where δ is the vertical thickness of the turbulent core based on the Thorpe-ordered profiles. Here L_{Th} values are approximately the same as the above forced-patch case, but d_{max} values are smaller. In this region, the turbulence is decaying and partially fossilized, and d_{max} cannot be expected to be as high as in forced turbulent patches.

6.5. *Interfacial-layer properties*

The interfacial layer plays an important role as a communication medium between the outer linearly stratified layer and the turbulent patch. In the experiment, the interfacial thickness was calculated by using the density gradient, $\mathrm{d}\rho/\mathrm{d}z$ (of the Thorpe-ordered profile) at the middle of the interfacial layer, viz. $\delta_i = \Delta\rho/(\mathrm{d}\rho/\mathrm{d}z)$, where $\Delta\rho = |\rho(0) - \rho(z_0)|$ is the interfacial density jump and z_0 is the location beyond which the Thorpe-ordered and undisturbed density profiles overlap. The results showed that the averaged interfacial-layer thickness δ_i varies with the size of the collapsing patch h_c as $\delta_i \simeq 0.03 h_c$.

Turbulence in the patch forces a field of internal waves trapped in the interfacial

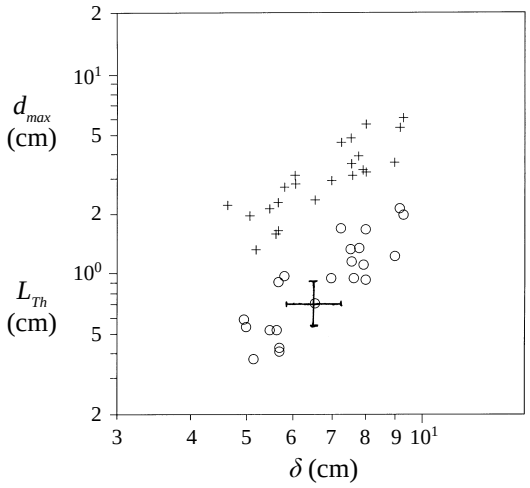

FIGURE 17. Variation of the Thorpe lengthscale L_{Th} and the maximum Thorpe displacement d_{max} with the vertical thickness of the turbulent core δ at various measurement locations along the intrusion. $S = 0.85$ cm and $23 < f/N < 62$.

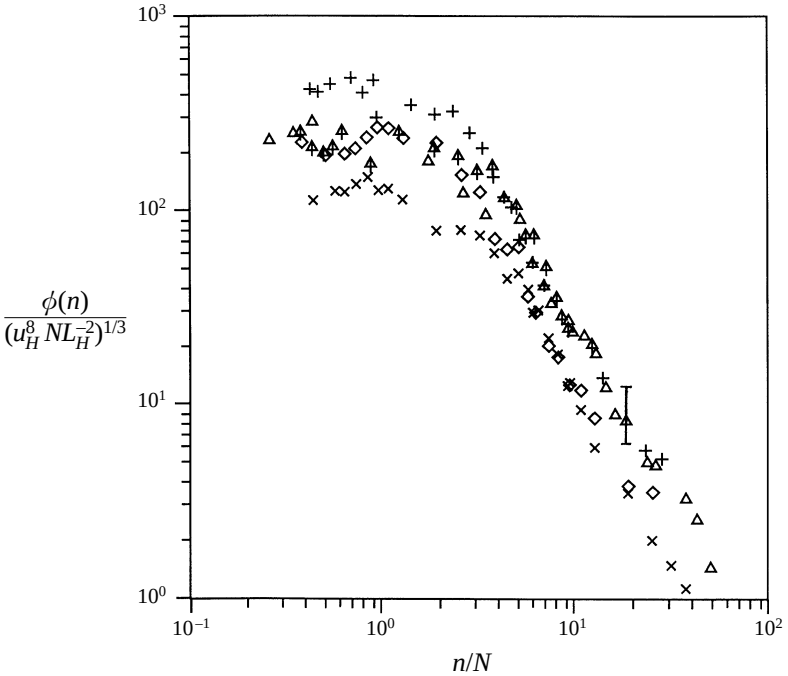

FIGURE 18. A plot of $\phi(n)/(u_H^8 NL_H^{-2})^{1/3}$ vs. (n/N) for five different experiments. The data show a good collapse for $n > 2N$. Note that $N_i \simeq 4N$ is the buoyancy frequency of the interfacial layer. $S = 1.18$ rad s^{-1} and $f/N = 28.8$.

layer (Fernando & Hunt 1997), which becomes saturated and degenerates into turbulence thus causing local mixing. As pointed out by E & Hopfinger (1986), these waves leak only a little energy to the outer stratified layer, because the waves break and dissipate energy at the interface itself. The fluctuations of buoyancy within the interfacial layer were measured at $x = 0$ using conductivity probes located at the interfacial region, and the corresponding spectra were calculated. Figure 18 shows a

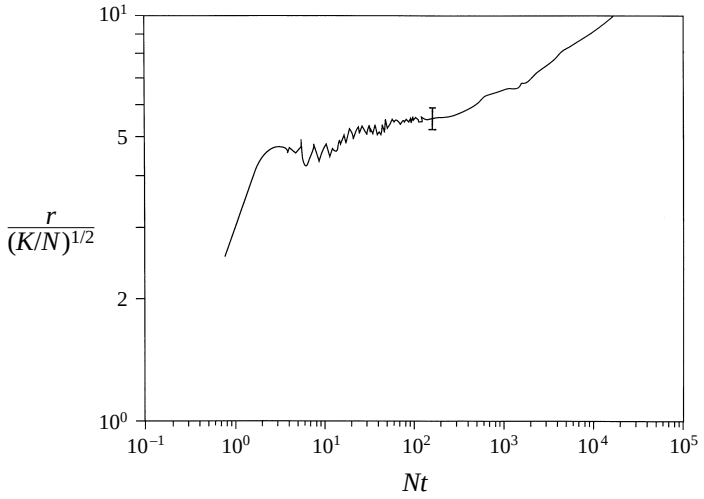

FIGURE 19. The growth of the normalized half-patch thickness with normalized time. $S = 0.85$ cm, $N = 1.18$ rad s^{-1} and $f/N = 28.8$.

comparison of measurements with the spectral form proposed by De Silva & Fernando (1992) for non-collapsing patches,

$$\frac{\phi(n)}{[u_H^8 N L_H^{-2}]^{1/3}} = \left[\frac{n}{N}\right]^{-5/3} \quad (n \gg N), \tag{12}$$

where $\phi(n)$ is the spectral density of buoyancy fluctuations. A satisfactory collapse of the data can be seen at higher frequencies, within the error margin of the measurements. This indicates that the presence of return currents at the corners of the patch does not have a significant influence on interfacial buoyancy fluctuations at the central part of the patch, possibly because of the entrainment of such currents before they reach the centre of the patch (figure 5*d*).

6.6. '*Subsequent growth*' *of the mixed region*

Figure 19 shows a typical plot of the growth of the half-patch thickness with time. These data were obtained from video images taken during the experiments; the data were taken at every 1 s up to $Nt \approx 200$ and at intervals of 60 s thereafter. Note the existence of several growth regimes. At $Nt < 4$, the growth follows $t^{1/2}$ behaviour, similar to one-dimensional growth of grid turbulence in homogeneous fluids (e.g. Dickinson & Long 1978); this was identified in §5 as the 'initial growth' regime. The mixed region then stays approximately at its limiting thickness r_c for some time before it starts growing again. During this period and thereafter, the thickness of the mixed patch fluctuates periodically; in §§5 and 6.3, this observation was attributed either to ejection of mixed fluid out of the patch and arrival of make-up fluid by the return currents or to the modulations introduced by background internal waves. Once the intrusion is blocked by the endwalls, the entire mixed region (the active turbulent patch and the side arm) grows in the vertical direction ('subsequent growth'); this evolution consists of two regimes, namely (i) a 'transient' subsequent growth regime characterized by the slow growth of the patch and the filling up of the side arm with collapsed fluid (figure 4*h*), and (ii) the 'final' subsequent growth regime wherein the side arm is filled and has approximately horizontal boundaries, with no visible sign of differential deepening between the patch and the side arm (figures 4*i*, and 5*h*, *i*).

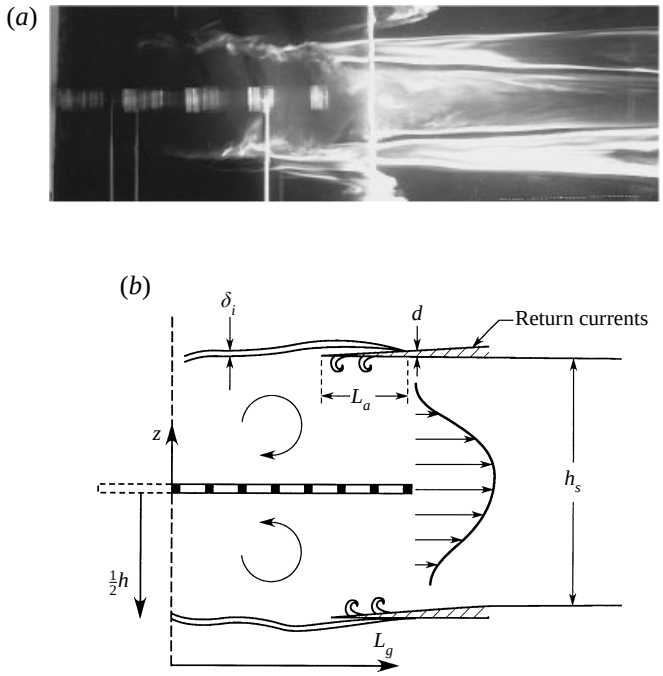

FIGURE 20. (*a*) A photograph depicting the mixing of return currents as they enter the patch. (*b*) A schematic of various features pertinent to the subsequent growth of the patch.

During 'transient' growth, delineation of a well-defined growth law of the form $r \sim t^m$, was difficult, because of strong fluctuations of the patch size. The best-fit line to the data in the range $10 < Nt < 2 \times 10^2$ show that $m = 0.12 \pm 0.2$; although this is close to $t^{1/9}$ or $t^{1/8}$ observed during the one-dimensional growth of a confined patch at large times (De Silva & Fernando 1992), the underlying physics of the two cases is not the same owing to the presence of strong return currents in the collapsing case. During 'final' growth, the fluctuation of r is much smaller because the vertical thickness of the side arm h_s is only slightly less than that of the patch h. This growth law takes the form $r \sim t^{1/5}$, which is different from that found by Maxworthy & Monismith (1985, 1988). They argued the entrainment rate for the subsequent growth is the same as the one-dimensional entrainment velocity multiplied by the fraction of the total length over which active mixing takes place (i.e. the length of the grid).

The disparity noted above can be attributed to the following. (i) the data of Maxworthy & Monismith (1985) mainly represent the transient regime during which (rather fortuitously) the entrainment power law is close to that of one-dimensional mixing experiments. (ii) There are subtle differences between their experimental configuration (figure 1(*c*)) and that of ours; they used a plate at the edge of the grid to suppress the vortex formation, which may have constrained the return currents. (iii) The observed entrainment law is sensitive to the position of the virtual origin. In the asymmetric geometry used by Maxworthy & Monismith (1985), the virtual origin did not coincide with the grid mid-plane from which their distances were measured (Hopfinger & Toly 1976).

To investigate the entrainment mechanism during the subsequent growth, extensive flow visualization studies were made and the results are outlined below.

(i) Although they appear to be the same over a shadowgraph (figure 5*i*), h is slightly

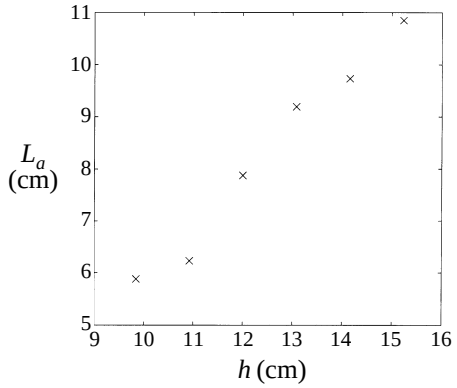

FIGURE 21. The variation of the intruding length L_a of the return currents into the patch with the thickness of the patch h.

larger than h_s. As h grows, $(h-h_s)$ becomes smaller, and the measurement of $(h-h_s)$ becomes increasingly difficult.

(ii) Thin return currents are still present and the fluid is ejected out of the patch (figure 5*h*). Evidently, the contribution to the mixed-layer growth by the return currents overshadows the contributions from wave breaking at the entrainment interface.

(iii) The return currents enter the patch at its corners and then roll up, possibly owing to shear instabilities, as shown in figure 20. This newly arrived buoyant fluid is first locally mixed and then rapidly entrained into the patch by turbulent eddies.

(iv) The return currents travel a distance L_a into the patch, which is proportional to the thickness of the patch h (and hence to the integral lengthscale of turbulence L_H), before the entrainment is completed; see figure 21.

(As stated in §3.1, additional experiments carried out with cylindrical patch geometries showed similar results, indicating the general applicability of the above observations). Note that the overall picture emerging from the above observations differs from that of Maxworthy & Monismith (1988), and suggests that the return currents make the dominant contribution to vertical mixing; i.e. interfacial mixing at the top and bottom boundaries of the patch is negligible compared to the mixing contribution made by the return currents.

It is possible to expect that the half-patch thickness is dependent on K, L_g, L, N and t; because of the two dimensionality of the problem, W can be considered unimportant, but if the wall influence (aspect-ratio) becomes significant, W should also enter the problem. Thus, in general

$$r = r(K, N, t, L_g, L, W), \tag{13}$$

or

$$\frac{r}{(K/N)^{1/2}} = \Pi(Nt, L_g/L, W/L, L/(K/N)^{1/2}), \tag{14}$$

where Π is a function. If return currents make the dominant contribution to the patch growth, then Π should be independent of L_g/L. As pointed out by Maxworthy & Monismith (1985, 1988), when the growth is governed by interfacial entrainment, $\Pi \sim (Nt)^{1/8}(Lg/L)^{1/8}$.

In order to check the above disparate notions, experiments were carried out keeping W, L and $(K/N)^{1/2}$ constant but with two grid sizes, $L_g = 30$ cm and 60 cm. Plots of

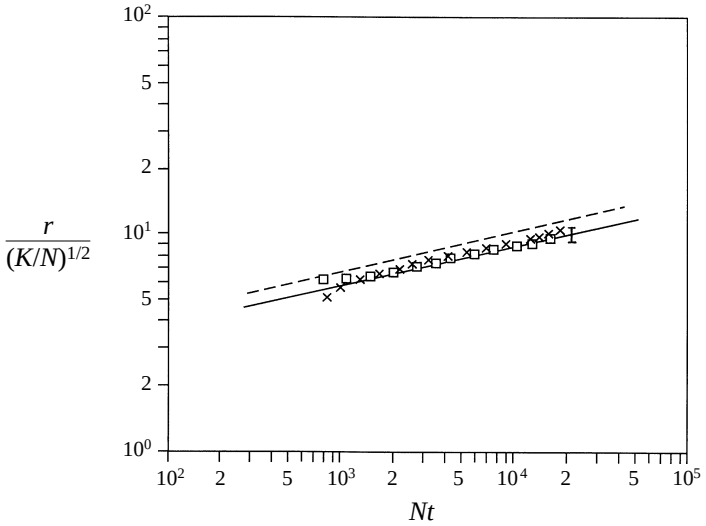

FIGURE 22. A plot of non-dimensional half-patch thickness versus non-dimensional time Nt for two different grid lengths. ×, $L_g = 60$ cm; ○, $L_g = 30$ cm.

$r/(K/N)^{1/2}$ vs. Nt for these experiments are shown in figure 22. The proposal by Maxworthy & Monismith (1985, 1988) implies that the entrainment rate for the large grid should be higher by a factor of $(L_g/L)^{1/8} \approx 1.10$; if the solid line in figure 22 corresponds to the smaller grid, the upper dashed line should represent the larger grid. The collapse of the data indicates that, within experimental error, there is no dependence of mixed-layer growth results on L_g/L; similar conclusions were reached in several sets of experiments carried out with different K/N. These results establish the fact that the 'final' growth phase is governed by return currents, and not by entrainment at the patch boundaries.

Entrainment model

In what follows, a simple entrainment model is developed to predict the final growth. Features relevant to the model development are depicted in figure 20(*b*), and the basic assumptions made in developing the model are:

(i) The flow is symmetric about (y, z)-plane, and the mixed-layer growth is essentially two-dimensional.

(ii) Non-turbulent fluid can be entrained into the patch either by wave breaking or via return currents, but the latter makes the dominant contribution. The return currents are entrained over a distance $L_a \propto h$ along the edges of the patch (figure 21).

(iii) The difference between the half-patch thicknesses and the side arm $d(=\frac{1}{2}(h-h_s))$ causes a horizontal pressure difference (per unit mass) of the order N^2d, which is responsible for the ejection of patch fluid into the side arm. This, in turn, induces return currents of which the thickness at the entrance to the path is d. The average velocity of the ejected fluid can be estimated as Nd, based on a buoyancy-inertia balance.

(iv) Since the return currents are responsible for replenishing 'lost' fluid from the patch, its velocity can be estimated as $c_r \sim (Ndh)/d \sim Nh$.

(v) The return currents spread over the density interface and the flow here is similar to a gravity current entering a turbulent environment (e.g. Thomas & Simpson 1985).

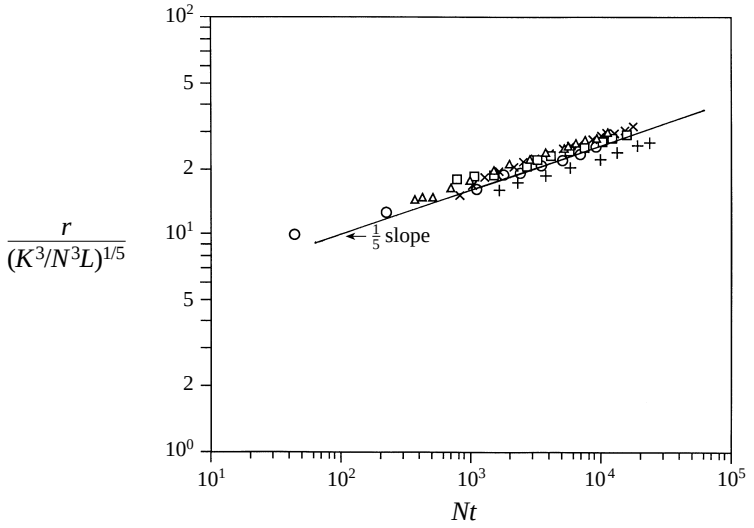

FIGURE 23. Comparison of mixed-layer growth data with the formulation (18); a plot of $r/(K^3/N^3L)^{1/5}$ vs. Nt. +, $K = 0.44$ cm^2 s^{-1}, $N = 1.27$ rad s^{-1}, $L_g = 30$ cm; ×, 0.99, 1.35, 30; ○, 1.30, 0.74, 60; △, 0.96, 0.69, 30; □, 0.89, 1.19, 30.

These currents can be incorporated into the patch by two mechanisms, namely, (i) The energy-containing eddies of the patch can engulf fluid from the return currents; or (ii) the return currents can locally mix with the patch fluid owing to shear instabilities. Mechanism (i) is untenable, because the size of the patch is now greater than the maximum eddy overturning scale r_c; hence the eddies are not sufficiently energetic to entrain directly from the return currents. On the other hand, the velocity and buoyancy jumps between counter-flowing return currents and the collapsed fluid are of the order $N(h-d) \sim Nh$ and N^2h, respectively; thus the local Richardson number based on the return current thickness d is $N^2hd/N^2h^2 \sim d/h \ll 1$, creating conditions for shear instabilities and local mixing (Narimousa & Fernando 1987). The locally mixed fluid, then, is engulfed into the patch by turbulent eddies with a characteristic velocity u_H.

(vi) Since the increase of potential energy of the system is a result of effective mixing over a length L_a, it is possible to extend Linden's (1975) entrainment hypothesis to the present flow situation; i.e. the rate of change of potential energy of the system is proportional to the kinetic energy flux available for mixing. The rate of change of potential energy (per unit width) of the system is given by

$$\frac{\mathrm{d}\Lambda}{\mathrm{d}t} = \tfrac{1}{4}L_g\rho_0 N^2h^2\frac{\mathrm{d}h}{\mathrm{d}t} + \tfrac{1}{4}(L-L_g)\rho_0 N^2h_s^2\frac{\mathrm{d}h_s}{\mathrm{d}t}, \tag{15}$$

or, since $d \ll h \sim h_s$, to the first approximation, it is possible to write

$$\frac{\mathrm{d}\Lambda}{\mathrm{d}t} = \tfrac{1}{4}L\rho_0 N^2h^2\frac{\mathrm{d}h}{\mathrm{d}t}. \tag{16}$$

The kinetic energy (per unit width) available for mixing can be parameterized as $\rho_0 u_H^3 L_a$, and using $L_a \propto h$, (16) becomes

$$LN^2h^2\frac{\mathrm{d}h}{\mathrm{d}t} \sim hu_H^3 \sim \frac{K^3}{h^2}, \tag{17}$$

where we have used (4). The entrainment law based on (17) can be written as

$$\frac{r}{(K^3N^{-3}L^{-1})^{1/5}} = \alpha(Nt)^{1/5}, \tag{18}$$

where α is a constant. Note that (18) predicts a faster growth rate than that of one-dimensional growth in confined geometries, because of more efficient mixing by return currents.

Figure 23 shows a plot of $r/(K^3N^{-3}L^{-1})^{1/5}$ versus Nt for a set of experiments conducted at different K, L_g and N. The collapse of the data and their power law behaviour provide strong support for the entrainment model presented above. Also, it is possible to evaluate $\alpha \simeq 4.0$.

7. Summary

The aim of the present study was to investigate the evolution of a continuously forced single turbulent patch in an unconfined stratified environment in the presence and absence of lateral boundary influence. The patch was allowed to collapse to form intrusions and the evolution of the patch/intrusion flow system was studied. Sustained turbulent patches are believed to be present in oceans (wherein boundary influence may be insignificant) and in lakes (where lateral boundaries play a role). More than one hundred and fifty experiments were performed, and the salient results are summarized below.

(i) The turbulent patch initially grows as in a non-stratified fluid for a dimensionless time $Nt \simeq 4$, when the growth is arrested by buoyancy forces. Thereafter, the mixed region collapses to form an intrusion at a dimensionless time $Nt \simeq 5$. The return currents are set up at the corners of the patch to replenish the fluid fed into the intrusion.

(ii) During the 'initial spreading' regime, the nose of the intrusion propagates with an average velocity c satisfying $c/Nr_c \simeq 0.15$, where r_c is the half-thickness of the patch and N is the buoyancy frequency. This propagation speed does not depend on viscous effects; the major resistance to the motion comes from the upstream-propagating zero- (or low-) frequency internal waves that leak energy from the intrusion. The viscous effects, however, become important in the flow upstream of the intrusion, where the viscous diffusion of vorticity causes the development of a slug of fluid pushed ahead of the intrusion.

Although the flow within the intrusion close to the patch is unsteady, the average nose speed is approximately constant. The fluctuation of the horizontal pressure gradient owing to the collapse of mixed fluid and arrival of return currents or the modulation of the patch thickness by background internal waves (or a combination thereof) can be the possible cause(s) for the unsteadiness.

(iii) Once the slug of fluid pushed ahead of the intrusion reaches the tank endwall, the intrusion speed is reduced sharply (blocking). The nose of the intrusion eventually arrives at the endwall. After the initiation of blocking, the patch and the intrusion grow vertically. Initially this growth is slow, and most of the collapsing fluid is used to fill in the intrusion to make its boundaries horizontal. In this 'transient' growth regime, $10 < Nt < 2 \times 10^2$, the patch thickness h grows as $h \sim t^m$, where $m = 0.12 \pm 0.2$. Continued collapse of fluid into the intrusion causes the thicknesses of the patch h and the side arm h_s to become comparable and their boundaries to be approximately horizontal. Then both h and h_s grow simultaneously, as if there is no differential

deepening. Detailed studies indicate that, though small, $h-h_s$ is dynamically significant in driving the return currents. The growth law for this final phase takes the form $h \sim t^{1/5}$.

(iv) The Thorpe lengthscale L_{Th} and the maximum Thorpe displacement d_{max} measurements within the turbulent patch are similar to those of non-collapsing (confined) forced patches. The measurements made within the decaying turbulent region, exterior to the patch, showed significantly different behaviour.

(v) Interfacial-layer parameters have similarities to those of non-collapsing patches, indicating similar interfacial mixing characteristics. The measurement of mixed-layer growth rates, however, did not confirm the previous notion of Maxworthy & Monismith (1988) that the rate of growth of the mixed region is the same as the product of the rate of growth of the mixed layer in the non-collapsing case and the fraction of the tank area occupied by the grid. The return currents feeding the patch overshadow the direct entrainment contribution of wave-breaking, and hence the former controls the mixed-layer growth. A simple model is developed to predict the 'final' phase of the mixed-layer growth, and the model predictions are in good agreement with the experimental results.

8. Discussion

For application purposes, it is of interest to calculate the eddy diffusivity of buoyancy associated with turbulent mixing within the patch. During the initial spreading regime, ambient fluid enters the patch via return currents is subjected to mixing and then is fed into the intrusion. The turbulence along the intrusion decays rapidly, and thus vertical mixing is confined to the patch. Assuming an approximately wedge-shaped intrusion fed by a turbulent patch of length L_g having horizontal boundaries and considering the rate of change of mass in upper/lower halves of the patch/intrusion about its horizontal mid-plane, it is possible to calculate the total buoyancy B per unit width crossing the horizontal plane of symmetry of the patch as

$$B = \tfrac{1}{3} N^2 r_c^2 \, c. \tag{19}$$

If the buoyancy transport is assumed to occur mainly within the active turbulent region of length L_g, the buoyancy flux can be evaluated as B/L_g, and thus the effective eddy diffusivity becomes

$$K_e = \frac{1}{3} \frac{r_c^2 \, c}{L_g}. \tag{20}$$

Using (5*a*), (6*a*) and (20), it is possible to obtain

$$K_e = 5.2 \left(\frac{K^3}{N L_g^2} \right)^{1/2}, \tag{21}$$

or using (3) and (4)

$$K_e \approx 1.65 \times 10^2 \left(\frac{\nu_t^3}{N L_g^2} \right)^{1/2}, \tag{22}$$

where $\nu_t = u_H L_H$ is the eddy viscosity within the patch. Using (22), an estimate can be made for K_e of sustained oceanic turbulent patches. Using typical parameters pertinent to oceanic patches, $L_g \simeq 20$ m, $N \simeq 8 \times 10^{-3}$ rad s^{-1} and $\nu_t \simeq 10^{-5}$ m^2 s^{-1}, it is possible to get $K_e \simeq 2.9 \times 10^{-6}$ m^2 s^{-1}; this is not far off the commonly quoted values for the thermocline in open ocean, $5 \times 10^{-6} < K_e < 5 \times 10^{-5}$ (m^2 s^{-1}) (Müller & Holloway 1989; also see Polzin *et al.* 1997).

If a similar calculation is made for diapycnal mixing during the subsequent 'final growth', it is possible to obtain

$$K_e = \left[\frac{L}{L_g}\right] h u_e, \tag{23}$$

where u_e is the entrainment velocity. Using (3) and (4), K_e becomes

$$K_e \approx 2 \times 10^5 \left(\frac{\nu_t^3}{L_g N^2 r_c^3}\right). \tag{24}$$

The expression (24) is especially applicable to boundary mixing situations, after the final growth regime is established.

The authors wish to thank Mr Leonard Montenegro for helping them in numerous ways, especially through his expertise in electronic instrumentation, and Drs P. A. Davies, D. F. Jankowski, G. Oth and F. Zangrando for their help in numerous ways. IPDeS would like to thank Professors Jorg Imberger and Greg Ivey for their encouragement. The financial support provided by the Office of Naval Research (High Latitude Dynamics and Physical Oceanography Programs) and the Fluid Mechanics Program of the National Science Foundation is gratefully acknowledged. Two anonymous referees provided helpful comments that led to a considerable improvement of the paper.

REFERENCES

Armi, L. 1978 Some evidence for boundary mixing in the deep ocean. *J. Geophys. Res.* **83**, 1971–1979.

Brandt, A., Sarabun, C. C., Seliger, H. H. & Tyler, M. A. 1986 The effects of the broad spectrum of physical activity on the biological processes in the Chesapeake Bay. In *Marine Interfaces Ecohydrodynamics* (ed. J. C. J. Nihoul), pp. 361–384.

Brandt, A. & Heijst, G. J. F. van 1987 Laboratory experiments on intrusive flow in a linearly stratified pycnocline. *Proc. 3rd Intl Symp. on Stratified Flows*, *Pasadena*, pp. 666–674.

Broutman, D. 1986 On internal wave caustics. *J. Phys. Oceanogr.* **16**, 1625–1635.

Caldwell, D. R. 1983 Oceanic turbulence: Big bangs or continuous creation? *J. Geophys. Res.* **88**, 7543–7550.

Caldwell, D. R., Brubaker, J. M. & Neal, V. T. 1978 Thermal microstructure on a lake slope. *Limnol. Oceanogr.* **23**, 372–374.

Casamitjana, X. & Roget, E. 1993 Resuspension of sediment by focused groundwater in Lake Banyoles. *Limnol. Oceanogr.* **38** (3), 643–656.

Caughey, S. J. 1982 Observed characteristics of the atmospheric boundary layer. In *Atmospheric Turbulence and Air Pollution Modelling* (ed. F. T. M. Nieuwstadt & H. Vandop), pp. 107–158.

Crawford, W. R. 1986 A comparison of length-scales and decay times of turbulence in stably stratified flows. *J. Phys. Oceanogr.* **16**, 1847–1854.

De Silva, I. P. D. 1991 Some studies in stratified turbulence. PhD dissertation, Arizona State University.

De Silva, I. P. D. & Fernando, H. J. S. 1992 Some aspects of mixing in a stratified turbulent patch. *J. Fluid Mech.* **240**, 601–625.

De Silva, I. P. D., Fernando, H. J. S., Eaton, F. & Hebert, D. 1996 Evolution of Kelvin–Helmholtz billows in nature and laboratory. *Earth Planet. Sci. Lett.* **143**, 217–231.

Dickinson, S. C. & Long, R. R. 1978 Laboratory study of the growth of a turbulent layer of fluid. *Phys. Fluids* **21**, 1698–1701.

Dillon, T. M. 1984 The energetics of overturning structures: Implications for the theory of fossil turbulence. *J. Phys. Oceanogr.* **14**, 541–549.

E, X. & Hopfinger, E. J. 1986 On mixing across an interface in stably stratified fluid. *J. Fluid Mech.* **166**, 227–244.

Fernando, H. J. S. 1988 The growth of a turbulent patch in a stratified fluid. *J. Fluid Mech.* **190**, 55–70.

Fernando, H. J. S. & Hunt, J. C. R. 1997 Turbulence, waves and mixing at shear-free density interfaces. Part 1. A theoretical model. *J. Fluid Mech.* **347**, 197–234.

Gargett, A. E., Osborn, T. R. & Nasmyth, P. W. 1984 Local isotropy and the decay of turbulence in a stratified fluid. *J. Fluid Mech.* **144**, 231–280.

Gibson, C. H. 1986 Internal waves, fossil turbulence and composite ocean microstructure spectra. *J. Fluid Mech.* **168**, 89–117.

Gregg, M. C. 1984 Persistent turbulent mixing and near-inertial waves. *Internal Gravity Waves and Small Scale Turbulence*, Hawaiian Winter Workshop (ed. P. Müller & R. Pujalet), pp. 1–24.

Hannoun, I. A., Fernando, H. J. S. & List, E. J. 1988 Turbulence structure near a sharp density interface. *J. Fluid Mech.* **189**, 189–209.

Head, M. J. 1983 PhD dissertation. University of California, San Diego.

Hopfinger, E. J. 1987 Turbulence in stratified fluids: A review. *J. Geophys. Res.* **92** (c5), 5287–5303.

Hopfinger, E. J. & Linden, P. F. 1982 Formation of thermocline in zero-mean-shear turbulence subjected to a stabilizing buoyancy flux. *J. Fluid Mech.* **114**, 157–173.

Hopfinger, E. J. & Toly, J.-A. 1976 Spatially decaying turbulence and its relation to mixing across density interfaces. *J. Fluid Mech.* **78**, 155–175.

Lemckert, C. J. & Imberger, J. 1995 Turbulence within inertia-buoyancy balanced axisymmetric intrusions. *J. Geophys. Res.* **100** (C11), 22649–22666.

Linden, P. F. 1975 The deepening of a mixed layer in a linearly stratified fluid. *J. Fluid Mech.* **71**, 385–405.

Long, R. R. 1978 Theory of turbulence in a homogeneous fluid induced by an oscillating grid. *Phys. Fluids* **21**, 1887–1888.

McDougall, T. J. 1979 On the elimination of refractive index variations in turbulent density stratified liquid flows. *J. Fluid Mech.* **98**, 83–96.

McEwan, A. D. 1983 Internal mixing in stratified fluids. *J. Fluid Mech.* **128**, 59–80.

McGrath, J. L., Fernando, H. J. S. & Hunt, J. C. R. 1997 Turbulence, waves and mixing at shear-free density interfaces. Part 2. Laboratory experiments. *J. Fluid Mech.* **347**, 235–261.

Manins, P. C. 1976 Intrusion into a stratified fluid. *J. Fluid Mech.* **74**, 547–560.

Marmorino, G. O. 1987*a* Observations of small scale mixing processes in the seasonal thermocline. Part 11 – Wave breaking. *J. Phys. Oceanogr.* **17**, 1348–1355.

Marmorino, G. O. 1987*b* Observations of small scale mixing processes in the seasonal thermocline. Part 1 – Salt fingering. *J. Phys. Oceanogr.* **17**, 1339–1347.

Maxworthy, T. & Monismith, S. G. 1985 Differential deepening of a mixed layer in a stratified fluid. *IAHR 21st Congress*, Env. Dyn. Ref., ED-85-105.

Maxworthy, T. & Monismith, S. G. 1988 Differential mixing in a stratified fluid. *J. Fluid Mech.* **189**, 571–598.

Müller, P. & Holloway, G. 1989 Parameterization of small-scale processes. *EOS* **70** (36), 818–820.

Narimousa, S. & Fernando, H. J. S. 1987 On sheared density interface of an entraining stratified fluid. *J. Fluid Mech.* **174**, 1–22.

Ozmidov, R. V. 1965 On the turbulent exchange in a stably stratified ocean. *Isv. Akad. Nauk SSSR Atmos. Okean. Phyz.* **1**, 493–497.

Pao, H.-P. & Kao, T. 1974 Dynamics of establishment of selective withdrawal of a stratified fluid from a line sink. Part 1. Theory. *J. Fluid Mech.* **65**, 657–688.

Perera, M. J. A. M., Fernando, H. J. S. & Boyer, D. L. 1994 Turbulent mixing at an inversion layer. *J. Fluid Mech.* **267**, 275–298.

Peyret, R. 1976 Unsteady evolution of a horizontal jet in a stratified fluid. *J. Fluid Mech.* **78**, 49–63.

Polzin, K. L., Toole, J. M., Ledwell, J. R. & Schmitt, R. W. 1997 Spatial variability of turbulent mixing in the abyssal ocean. *Science* **276**, 93–96.

ROBERTS, P. J. W. & MATTHEWS, P. R. 1986 Behavior of low-buoyancy jets in a linearly stratified fluid. *J. Hydraul. Res.* **25** (4), 503–519.

STILLINGER, D. C., HELLAND, K. N. & VAN ATTA, C. W. 1983 Experiments on the transition of homogeneous turbulence to internal waves in a stratified fluid. *J. Fluid Mech.* **131**, 91–122.

THOMAS, N. H. & SIMPSON, J. E. 1985 Mixing of gravity currents in turbulent surroundings: Laboratory studies and modelling implications. In *Turbulence and Diffusion in Stable Environments* (ed. J. C. R. Hunt), p. 61, Clarendon.

THORPE, S. A. 1977 Turbulence and mixing in a Scottish loch. *Phil. Trans. R. Soc. Lond.* A **286**, 125–181.

TRITTON, D. J. 1977 *Physical Fluid Dynamics*. Van Nostrand Reinhold, Wokingham.

WONG, K. K. & KAO, T. W. 1970 Stratified flow over extended obstacles and its application to topographical effect on vertical wind shear. *J. Atmos. Sci.* **27**, 884–889.

WOODS, J. D. 1968 Wave-induced shear instability in summer thermocline. *J. Fluid Mech.* **32**, 791–800.

WU, J. 1969 Mixed region collapse with internal wave generation in a density-stratified medium. *J. Fluid Mech.* **35**, 531–544.